VOLUME 73, NUMBER 10, OCTOBER 2019

EVOLUTION

INTERNATIONAL JOURNAL OF ORGANIC EVOLUTION

SSE

SOCIETY *for the* STUDY *of* EVOLUTION

ORIGINAL ARTICLE

doi:10.1111/evo.13834

SSE SOCIETY for the STUDY of EVOLUTION

EVOLUTION INTERNATIONAL JOURNAL OF ORGANIC EVOLUTION

Evolution of aerial spider webs coincided with repeated structural optimization of silk anchorages

Jonas O. Wolff,[1,2] **Gustavo B. Paterno,**[3,4] **Daniele Liprandi,**[5] **Martín J. Ramírez,**[6] **Federico Bosia,**[7] **Arie van der Meijden,**[8] **Peter Michalik,**[9] **Helen M. Smith,**[10] **Braxton R. Jones,**[1] **Alexandra M. Ravelo,**[6] **Nicola Pugno,**[5,11,12] **and Marie E. Herberstein**[1]

[1]Department of Biological Sciences, Macquarie University, Sydney, New South Wales 2109, Australia

[2]E-mail: jonas.wolff@mq.edu.au

[3]Departamento de Ecologia, Centro de Biociências, Universidade Federal do Rio Grande do Norte (UFRN), Lagoa Nova, 59072–970, Natal, Rio Grande do Norte, Brazil

[4]Instituto de Ciências Biológicas, Programa de Pós-Graduação em Ecologia, Universidade Federal de Juiz de Fora, Rua José Lourenço Kelmer, 36036–900, Juiz de Fora, Minas Gerais, Brazil

[5]Laboratory of Bio-Inspired and Graphene Nanomechanics, Department of Civil, Environmental and Mechanical Engineering, University of Trento, Via Masiano 77, I-38123, Trento, Italy

[6]Museo Argentino de Ciencias Naturales "Bernardino Rivadavia", Consejo Nacional de Investigaciones Científicas y Técnicas (CONICET), Av. Ángel Gallardo 470, C1405DJR, Buenos Aires, Argentina

[7]Department of Physics and Nanostructured Interfaces and Surfaces Interdepartmental Centre, Università di Torino, Via P. Giuria 1, 10125 Torino, Italy

[8]CIBIO Research Centre in Biodiversity and Genetic Resources, InBIO, Universidade do Porto, Campus Agrário de Vairão, Rua Padre Armando Quintas, Vairão, Vila do Conde, Porto, 4485–661, Portugal

[9]Zoologisches Institut und Museum, Universität Greifswald, Loitzer Str. 26, 17489, Greifswald, Germany

[10]Australian Museum, 1 William St, Sydney, New South Wales, 2010, Australia

[11]School of Engineering and Materials Science, Queen Mary University, Mile End Rd, London E1 4NS, UK

[12]KET Labs, Edoardo Amaldi Foundation, Via del Politecnico snc, 00133, Rome, Italy

Received April 14, 2019
Accepted July 25, 2019

Physical structures built by animals challenge our understanding of biological processes and inspire the development of smart materials and green architecture. It is thus indispensable to understand the drivers, constraints, and dynamics that lead to the emergence and modification of building behavior. Here, we demonstrate that spider web diversification repeatedly followed strikingly similar evolutionary trajectories, guided by physical constraints. We found that the evolution of suspended webs that intercept flying prey coincided with small changes in silk anchoring behavior with considerable effects on the robustness of web attachment. The use of nanofiber based capture threads (cribellate silk) conflicts with the behavioral enhancement of web attachment, and the repeated loss of this trait was frequently followed by physical improvements of web anchor structure. These findings suggest that the evolution of building behavior may be constrained by major physical traits limiting its role in rapid adaptation to a changing environment.

KEY WORDS: Animal architecture, bio-inspiration, evolutionary biomechanics, extended phenotype, macro-evolution, spider silk.

Evolution 73-10: 2122–2134

From efficient tunnel networks of ant colonies and strikingly effective thermal control of termite mounds to the aesthetic assembly of bower bird displays and ecosystem-forming beaver dams: the complexity, efficiency, and far reaching effects of animal buildings excite and inspire (Hansell 2005)—their study may even drive technical innovation toward a greener future (Turner and Soar 2008). Our understanding of how building behavior evolves within an ecological context is limited because animal architectures blur the boundaries of an organism's phenotype (Dawkins 1982; Odling-Smee et al. 2003; Bailey 2012).

Spider webs are flagship examples of animal architectures, and their enormous diversity in shape render them an ideal system in which to unravel the evolutionary dynamics of building behavior. Hypotheses of spider web evolution have been formulated for more than a hundred years, with a focus on the role of putatively singular events, such as the emergence of distinct building routines, specific silk proteins, or viscid silk (Coddington 1986; Eberhard 1990; Bond and Opell 1998; Coddington 2005; Blackledge et al. 2009). In contrast, recent (Bond et al. 2014; Fernández et al. 2014; Fernández et al. 2018) and controversial (Garrison et al. 2016; Eberhard 2018) phylogenomic studies favor a more dynamic scenario, where similar behavioral routines have repeatedly evolved. The core of the controversy is the question whether the evolution of behavioral building routines is dynamic and repeatable or slow and determined by contingent events. The answer to this question goes beyond spider webs: if the evolution of behavior is less constrained than the evolution of physiological and morphological traits it could facilitate rapid responses to environmental changes, thereby setting the course of evolutionary trajectories (West-Eberhard 1989; Wcislo 1989; Odling-Smee et al. 2003; Ord and Summers 2015).

Here, we approach the inference of spider web evolution from a previously neglected angle: the idea that a robust foundation is the basis for a stable building (Hansell 2005). It has been proposed that the evolution of tape-like thread anchorages at the base of modern spiders (Araneomorphae) ~300 million years ago dramatically changed silk usage: spiders were no longer restricted to spinning substrate-bound sheets, but could produce complex three-dimensional structures by spatially arranging single lines (Coddington 2005; Wolff et al. 2017). Despite this early insight, subsequent work has focused on the role of web geometry and silk proteins in the evolution of webs, neglecting the role of web anchorages.

Web anchors are tape-like silk films built of glue-coated silk nanofibers produced by a special type of silk gland, the "piriform" gland (Kovoor 1987; Wolff et al. 2015; Wirth et al. 2019). The openings of the numerous small piriform glands are grouped on the tip of the second pair of spinnerets (the "anterior lateral spinnerets") around one or few openings of the large "major ampullate" glands, which produce the silk thread ("dragline") used to build the web scaffold (Eberhard 2010). The rubbing of the paired spinnerets against each other and on the substrate forms the stable attachment of the dragline (Eberhard 2010; Wolff et al. 2015). These spinneret movements follow a stereotyped choreography that determines the resulting structure of the anchor (Wolff et al. 2017; Fig. 1).

Since anchor strength underlies global mechanical rules, it is possible to derive parameter estimates for its physical optimization (Pugno et al. 2013). A previous parametric study by two of us revealed that a single parameter in anchor structure (i.e., the location of the dragline joint) explains most of the variation in anchor strength (Wolff and Herberstein 2017). We hypothesized that lineages that achieve optimal anchor strength by behavioral means, also achieve web types with greater mechanical integrity. To test this, we quantified silk anchor structure and web types in 105 spider species of 45 families, covering all major clades of the modern spiders. We first built a numerical model to identify the optimum in anchor structure and tested if it matched the adaptive peaks in the macro-evolutionary signal. We then related silk anchor performance to anchor building behavior and the morphology of the spinning apparatus. Specifically, we tested how the innate spinneret choreography during anchor production affects anchor structure, and how the configuration of the spinning apparatus affects the kinematic properties of the system. Here, we distinguished between such spiders that bear a spinning plate, the so-called "cribellum" (which is homologous to the first pair of spinnerets), in the anterior part of the spinning apparatus (cribellate spiders) and such, in which this organ is reduced and nonfunctional (ecribellate spiders). The cribellum is used to produce sophisticated adhesive capture threads, representing bundles of nanofibers, and we hypothesized that it restricts the mobility of the spinnerets involved in silk anchor production. Finally, we aimed to determine the sequence of silk anchor enhancement and aerial web evolution: did an evolutionary enhancement of silk anchors occur after the evolution of aerial webs, or did enhanced anchors precede the evolution of aerial webs? Such time sequences could provide insights into whether silk anchor mechanics constrain or facilitate the evolution of web architectures.

Materials and Methods

MATERIAL SOURCING AND FIELDWORK

Spiders were collected in Eastern Australia (NSW, QLD, VIC, and TAS), New Zealand (North Island), Germany, Italy, the United States of America, Argentina, and Morocco, or obtained from laboratory stocks (three species) and kept in the laboratory in plastic jars or boxes with slightly moistened tissue (complete list of species and collection data in Table S9). We aimed for three individuals per species, while we did not expect differences in our target traits between sexes and developmental stages

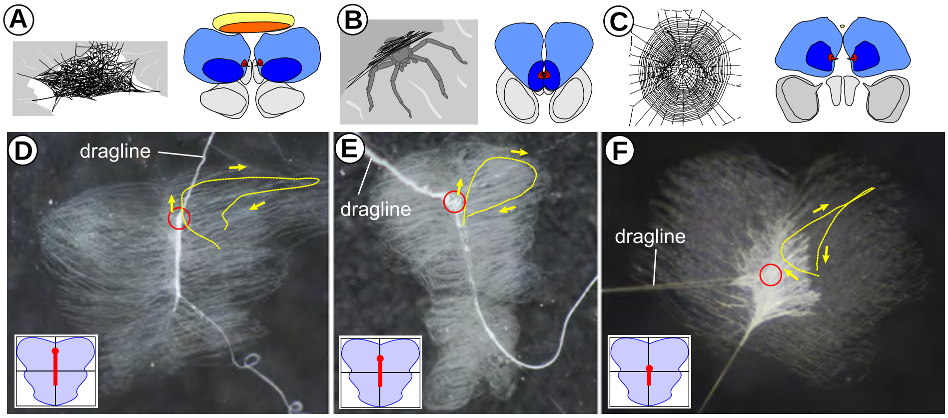

Figure 1. Variation of silk anchors. (A–C) Schematic illustration of silk use and ventral view of spinning apparatus for exemplary spider species. Anterior lateral spinnerets are coloured in blue, with the tip that bears the array of piriform glands in dark blue and the major ampullate gland spigot in red. The cribellum (if present) is coloured in yellow. (A) Substrate bound web and cribellar spinning apparatus of the Tasmanian cave spider *Hickmania troglodytes* (Austrochilidae), a representative of a basal lineage of araneomorph spiders. (B) Silk shelter and ecribellar spinning apparatus of the huntsman spider *Isopeda villosa* (Sparassidae), an arboreal hunting spider. (A) Orb web and ecribellar spinning apparatus of the St Andrew's cross spider *Argiope keyserlingi* (Araneidae), a derived aerial web builder. (D–F) Microscopy photos of silk anchors. The red circle indicates the point, where the load is transmitted from the upstream dragline onto the anchor (loading point). The movement track travelled by the left anterior lateral spinneret is overlaid in yellow with arrows indicating the direction of movement. The track shape represents the mean shape of movement units from 15 recordings (three individuals with five spinning events each). For this study the width-to-height ratio of such movement units was measured. To complete an anchor, usually a number of such movements are performed along the longitudinal axis of the anchor (for details, see Wolff et al. (2017)). In the lower left corner, a schematic overview about the depicted anchor demonstrates the differences in dragline joint placement (fused dragline in red). Anchors and spinning tracks are shown for (D) *H. troglodytes*, (E) *I. villosa*, and (F) *Eriophora* sp. (Araneidae).

(confirmed by intraspecific comparison of anchor structure in *Argiope keyserlingi* and *Nephila plumipes*, unpublished data). However, for some species, only single individuals could be obtained (samples sizes are given in Table S9 and Fig. 3). Silk samples were collected on glass slides that were left in the enclosures for 2–7 days. Silk samples were stored in dry boxes and are deposited at the Department of Biological Sciences, Macquarie University (MQ). Voucher specimens of spiders are deposited at the Australian Museum (AM), the Zoological Museum of the University of Greifswald (UG), the Natural History Museum of Argentina (MA), Canterbury Museum (CM), and private collections (see Table S9 for details).

For each species, we recorded the web type based on field and laboratory observations: 0, no web (hunting spider); 1, substrate bound web (capture area ± parallel and directly attached to the substrate surface); and 2, aerial web (capture area suspended, indirectly attached to substrate, and its shape ± independent of substrate topography). These categories were chosen, because they represent different demands of a robust anchorage.

MORPHOLOGY OF SPINNING APPARATUS

Spiders were investigated under dissection microscopes to score two states of the spinning apparatus: 0, ecribellate; 1, cribellate.

KINEMATICS OF SPINNING APPARATUS

Spinning choreography was studied in a subset of 71 species following the methods described in (Wolff and Herberstein 2017), using a Basler Ace 640 × 480pix USB 3.0 high speed video camera (Basler AG, Ahrensburg, Germany), equipped with a Navitar Precise Eye extension tube including a 1.33× magnification lens (Navitar, Inc., Rochester, NY, USA). A 0.25× accessory lens was used for larger spiders (body length > 10 mm). The resulting field of view was 1.3 × 1.0 mm at a pixel size of 2.1 µm for the basic configuration, and 5.3 × 4.0 mm at a pixel size of 8.3 µm for the configuration with the 0.25× lens. Videos were recorded with 500 frames/s, using the *TroublePix* software (NorPix, Inc., Montreal, QC, Canada) with continuous looping and post event trigger.

Videos were processed with *ImageJ* 1.5 (Schneider et al. 2012) as detailed in (Wolff and Herberstein 2017). The movements of both anterior lateral spinnerets were manually tracked using the *MTrackJ* plugin (Meijering et al. 2012), taking the center of the piriform spigot field on the anterior lateral spinneret apex as a reference. Each spinning sequence consists of a set of stereotypic spinneret trajectories. Single trajectories were extracted, their tracking coordinates positioned in a generalized grid and partitioned into 50 landmarks defined by regularly spaced time intervals (for details on this procedure we refer to Wolff and Herberstein 2017; Wolff et al. 2017). This procedure ensures that the relative orientation of the kinematic track shapes toward the animal's body axis is maintained. From these shapes, we calculated the relative track proportions h_r as the y-dimension divided by the x-dimension of the aligned track shape, where the minimal x-coordinate denotes the proximal turning point of the adducted spinneret (where the dragline is usually placed) and the maximal x-coordinate the lateral turning point of the abducted spinneret. This variable reflects under which angle piriform silk is spread away from the dragline joint.

The final dragline location may not only be determined by the trajectories of single kinematic elements, but also how these are applied along the animal's body axis. Some spiders perform a back-and-forth movement of the abdomen to further modulate dragline placement. This behavior was recorded as a binary character: 0, absent; 1, present.

STRUCTURE AND MORPHOMETRICS OF SILK ANCHORS

Nine to 20 silk anchors per individual spider were imaged with Leica M205A (Leica Microsystems GmbH, Wetzlar, Germany) and Motic (Motic Inc. Ltd., Hong Kong) stereo microscopes with mounted cameras.

Morphometrics of silk anchors was performed on micrographs in *ImageJ*. We calculated the dragline placement variable c_d as follows: distance d between the dragline joint (point where the dragline leaves the anchor) and the anterior border of the anchor divided by the longitudinal dimension of the anchor. In anchors of some basal species, the individual dragline fibers do not leave the anchor as a bundle, but separately in different locations. In these cases, the pair of fibers located closest to the frontal border of the anchor was taken into consideration and their d-values were averaged. Details on the morphometric characterization of silk anchors are described in Wolff and Herberstein (2017).

NUMERICAL MODEL

The elastic membrane was modeled by discretizing it in a network of elastic bonds (i.e., springs) in a square-diagonal lattice, using a generalized nonlinear 3D co-rotational truss formulation (Cook et al. 2001). A homogenization procedure was adopted, imposing the equivalence of the strain energy density of the lattice with that of a corresponding homogeneous membrane (Ostoja-Starzewski 2002; Brely et al. 2015). We used a standardized anchor geometry with length $l = 1$ mm, width $w = 1$ mm, thickness $t = 1$ µm, and with the dragline fused with the membrane over a length of $c_l = 0.33$ mm. To account for differences in silk properties, we performed separate simulations for a combination of membrane and dragline stiffness values, as empirically observed in the basal sheet web spider *H. troglodytes* and the aerial web builder *N. plumipes*: Young's modulus of piriform silk membrane $E_p = 0.25$ GPa for *Hickmania* and $E_p = 1.7$ GPa for *Nephila* (see tensile test methodologies and results in Supporting Information 1), and Young's modulus of dragline $E_d = 10$ GPa for *Hickmania* and $E_d = 15$ GPa for *Nephila* (after Swanson et al. 2006 and Piorkowski et al. 2018).

The interface was modeled assuming a 3D exponential-like traction-separation law (cohesive zone model) of the form $T_i = \Delta_i \frac{\phi_i}{\delta_i^2} \cdot \exp(\sum_j -\frac{\Delta_j^2}{\delta_j^2})$, where ϕ_i, Δ_i, and δ_i are the work of separation, the crack gap value, and the characteristic length (i.e., the gap value corresponding to the maximum traction; Salehani et al. 2018). The resulting system of coupled nonlinear equations in matrix form was solved using an algorithm based on the Newton–Raphson method (Ostrowski 1973) implemented in C++ and run on the OCCAM HPC cluster at the University of Torino. The adhesive energy of the interface, calculated as the integral of the cohesive law, was taken to be equal to $\phi = 0.5$ MPa·mm.

We simulated the maximal pull-off forces for different c_d between 0.0 and 0.5. To further study the effect of c_d on anchor robustness, we simulated maximal pull-off forces for different pull-off angles (loading angles) between 15° (± parallel to substrate along spinning direction) and 165° (± parallel to substrate against spinning direction, e.g., dragline flipped over) for a c_d of 0.0, 0.2, and 0.4.

PHYLOGENETIC INFERENCE

The phylogenetic tree was estimated using three mitochondrial (12S, 16S, COI) and three nuclear (histone H3, 18S, 28S) markers, taken from the study of Wheeler et al. (2017) and supplemented with sequences from GenBank (Table S11). The clades obtained as monophyletic in the genomic analyses of Fernández et al. (2018) (Araneae), Kallal et al. (2018) (Araneidae), Cheng and Piel (2018) (oval calamistrum clade), and Maddison et al. (2017) (Salticidae) were constrained for monophyly, as a backbone tree. The reason for such constrained analysis is that our six-marker dataset will not have sufficient signal to overturn the results based on hundreds to thousands of markers from the genomic analyses.

We lacked sequence data for 58 of the studied species but were able to use sequences from closely related species to obtain a good estimate of phylogenetic placement and branch lengths (Table S10). For an additional set of 20 species, we did not have close relatives, or a close relative was already in the dataset; these were connected randomly in internal branches according to their taxonomic placement (Table S10). Two non-araneomorph terminals were added to root the tree, representing the lineages Mesothelae and Mygalomorphae; these were excluded from the comparative analyses.

Alignment of sequences was performed with *MAFFT* version 7 online service (Katoh et al. 2017). Model selection was made with *jModeltest* (Darriba et al. 2012). Secondary dating of main tree nodes was assigned as mean and 95% HPD taken from

Fernández et al. (2018) and analyzed in *BEAST2* (Bouckaert et al. 2014) under a relaxed lognormal clock model (Drummond et al. 2006) and Yule tree prior, using the CIPRES Science Gateway (Miller et al. 2010b) for 50 million generations. After a pilot run, GTR models were simplified to HYK to achieve convergence. The 20 species without sequence data were free to connect anywhere along any branch within taxonomically constrained clades. For example, the four species of *Arkys* were constrained to form a monophyletic genus, even when we had sequences for two species only. To avoid for very short tip branches, we placed a uniform prior for the clade age, with minimum two million years ago for congeners and five million years ago for higher taxa.

To account for the uncertainty of the phylogenetic estimation, we obtained 100 trees randomly drawn from the post-burnin posterior sample of the Bayesian analysis in *BEAST2*. The subsequent comparative analyses are averaged over these 100 trees, and thus incorporate the uncertainty in phylogenetic parameters.

MACRO-EVOLUTIONARY FRAMEWORK

We used phylogenetic comparative methods to infer adaptive peaks and constraints and test evolutionary associations of silk anchor structure, spinning apparatus, spinning kinematics, and web building behavior, using multiple packages in the software environment *R*.

To select the best model for ancestral character estimation (ACE), we calculated the corrected Akaike information criterion weights (AICcw) using *geiger* 2.0.6 (Pennell et al. 2014). For spinning apparatus state, we fitted an Equal Rates model (ER), an All Rates Different model (ARD) and a customized model with suppressed state 1 to 2 transitions (following Dollo's law, see (Alfaro et al. 2018)), of which the Dollo's law model had the strongest support ($AICcw = 0.640$). For web type, ER, SYM, and ARD models were fitted, of which the ER model was preferred ($AICcw = 0.583$). ACE was performed with stochastic character mapping in *phytools* (Revell 2012), on the consensus tree with 100 repeats and across a sample of 100 trees with one simmap per tree.

To infer evolutionary dynamics of the continuous variables dragline placement c_d and spinning track dimensions h_r we used a multi-step model-selection process. To test if changes in discreet characters led to differential evolutionary dynamics, we fitted different Brownian Motion (BM) and generalized Ornstein–Uhlenbeck-based Hansen models (OU) using the package *OUwie* 1.50 (Beaulieu and O'Meara 2014). We built a set of models for spinning apparatus state (c) and web type (w, web type was binary discretized for this purpose in aerial web: 0, no; 1, yes) using a randomly drawn simmap of c- and w-regimes for each of the 100 trees from our sample. We tested a single-regime BM (*BM1*) and OU model (*OU1*), and per regime type each a two-σ^2 (*BMS*) BM model, and OU models with two θ (*OUM*), two θ and two σ^2 (*OUMV*), two θ and two α (*OUMA*), and two θ, two σ^2, and two σ^2 (*OUMVA*). The *AICcw* was used to compare the fit between all 12 models for each tree. *AICcw* and model parameters were then summarized across all 100 trees and their median and variance assessed to select for the model(s) that could best explain the data. For each c_d and h_r, we ran two loops across the tree sample to check for the effect of the stochastic component in this procedure, and found comparable results (i.e., similar models were favored and no major differences in median parameter estimates).

While prior clade assignments are useful to compare defined groups, they may miss some hidden patterns caused by unstudied effects. We therefore additionally used the methods *SURFACE* (Ingram and Mahler 2013) and *bayou* (Uyeda and Harmon 2014) on the consensus tree (Supporting Information S3). *SURFACE* performs stepwise AIC estimation to identify regime shifts in θ assuming evolution under the OU process with constant σ^2 and α. *bayou* uses a reverse-jump Markov chain Monte Carlo procedure for the similar purpose. By this, we also checked, if evolution of our variables was driven by singular events (i.e., the occurrence of only a single shift), which may bias PGLS inference (Uyeda et al. 2018). Priors in *bayou* analyses were defined as follows: for α, a half-Cauchy distribution with scale $= 0.1$; for σ^2, a half-Cauchy distribution with scale $= 0.01$; for θ, a uniform distribution delimited by $min = 0$ and $max = 1$; and a conditional Poisson for the number of shifts. Because the results of *bayou* can be sensitive to the mean number of shifts in the prior (Ho and Ané 2014; Uyeda and Harmon 2014), we ran each two chains over 500,000 generations for prior means of 10, 15, 20, and 25 shifts with equal shift probability and one shift maximum per branch, discarding the first 30% as burn-in. For c_d chains with priors of 20 and 25 shifts and for h_r chains with priors of 15, 20, and 25 shifts arrived at a similar posterior (Supporting Information S6). Results are reported from these chains only (means of converged chains given, and graphical representation of shifts for c_d from a randomly chosen chain with a prior of 25 shifts and for h_r from a randomly chosen chain with a prior of 20 shifts).

TRAIT CORRELATION

To reveal patterns of trait correlation, we used phylogenetic generalized least squares models (PGLS), which accounts for the non-independence of observations due to common evolutionary history (Felsenstein 1985; Grafen 1989; Freckleton et al. 2002), across pairwise combinations of our variables: (1) $c_d \sim$ *spinning apparatus*; (2) $c_d \sim$ *web type*; (3) $h_r \sim$ *spinning apparatus*; and (4) $h_r \sim$ *web type*. Further, we performed PGLS regressions between $c_d \sim h_r$. PGLS analyses were performed with the R package *phylolm* (Tung Ho and Ané 2014) and branch length transformation were optimized by setting *lambda* value through maximum likelihood. To account for phylogenetic uncertainty in PGLS results (Donoghue and Ackerly 1996), we repeated each model across our posterior sample of 100 phylogenetic trees. The influence of phylogenetic uncertainty on results was estimated by the variation in model parameters across all runs. Phylogenetic sensitivity analyses were performed for each PGLS model with the R package *sensiPhy* (Paterno et al. 2018).

GEOMETRIC MORPHOMETRICS

To test if the shape of spinning paths differed between spiders with different spinning apparatus and web type, and if it correlates with c_d and h_r, geometric morphometrics was performed using the R package *geomorph* (Adams and Otárola-Castillo 2013). For this purpose, aligned spinneret trajectories were discretized into 50 landmarks with similar time steps, as described in Wolff et al. (2017). We used both an alignment toward the median axis between the paired spinnerets, which keeps the angular orientation of the trajectories (see Wolff et al. 2017), and General Procrustes Alignment (GPA), which omits this information and extracts the pure shape. We then performed Phylogenetic Procrustes ANOVA against the variable "spinning apparatus" and "web type" and Phylogenetic Procrustes Regression against variables c_d and h_r using the consensus tree.

Results

PHYSICAL CONSTRAINTS AND OPTIMA OF SILK ANCHORAGES

Our broad comparative study of anchor structures across the spider tree of life confirmed that there is a general structure of web anchors, consisting of a dragline attached to the substrate with numerous, sub-micron sized, glue coated fibers (piriform silk) combined into a patch-like film. The major interspecific differences are the shape of the piriform silk film and the structure of the dragline joint (Fig. 1D–F). The dragline can be embedded all the way through this film, or be attached centrally only. The attachment position of the dragline greatly affects where and how load is transmitted onto the underlying film. The more central the dragline placement c_d (i.e., the more pronounced dragline joint centrality) the better the anchor can withstand stress from a variably loaded silk line. Preliminary studies have revealed that this is the most significant determinant of web anchor robustness (Wolff and Herberstein 2017).

To identify the optimum of the dragline placement parameter, we built a numerical model based on the theory of thin film contact mechanics (Pugno 2011), approximating silk anchorages as tape like films. Previous models of web anchor mechanics, such as the staple-pin model (Sahni et al. 2012; Pugno et al. 2013), do not account for the observed variation in dragline joint structure and presume independent peeling events of single piriform fibres, which, however, have not been empirically observed in peel-off tests with attachment discs from orb web spiders (Araneidae) and wandering spiders (Ctenidae) (Wolff et al. 2015; Wolff 2017; Wolff and Herberstein 2017). In our comparative analysis reported here, we did not observe a single case of an attachment disc composed of parallel piriform fibers that did not overlap with each other, confirming that the staple-pin model is not appropriate to describe the mechanics of spider web anchorages. We therefore developed a new model, approximating the piriform silk film as a single tape-like element, where load is shared and transmitted between piriform fibers.

To apply our results to a range of silk properties found in spiders, we repeated simulations for parameters measured in the Tasmanian cave spider (*Hickmania troglodytes*), representing an ancient lineage, and in golden orb web spiders (*Nephila plumipes*), a representative of derived aerial web builders. We found that anchor strength improved if its geometrical structure is allowed to maximize the peeling line (total length of the detachment front) before detachment, which occurred in the range $c_d = 0.3$–0.5 mm/mm for typical anchorage parameters (Fig. 2A). The exact optimum within this range depends, among others, on the material properties of the silk. For draglines as stiff as the anchor silk (or point-like dragline joints) $c_d = 0.5$ which decreased with an increase in stiffness difference between dragline and anchor silk. During detachment, the stress concentrations and subsequent delamination front approximated a circular shape that became more elliptical as the peeling angle increased (Fig. 2B). The dragline placement c_d determined a delay in the detachment front reaching the anchorage edges (for typical anchorage shapes), leading to an overall increase in robustness. This is in agreement with empirical data on silk anchors of orb web spiders (Supporting Information S2) and upscaled physical models (Wolff and Herberstein 2017). Notably, the effect of the pulling angle on anchor resistance was reduced at a high dragline joint centrality c_d (Fig. 2C and D). This indicates that the benefit of high c_d is realized in dynamic loading situations, such as in aerial webs.

EVOLUTIONARY DYNAMICS OF SPIDER WEB TRAITS

Spider webs are diverse in shape and function but for the purpose of our analyses, we categorized the web phenotypes into: "substrate webs," "aerial webs," and "webless foragers" (see Materials and Methods for definition). Aerial webs were hereby characterized by a capture area (sheet or tangle) that is fully suspended (i.e., indirectly attached to the substrate by supporting lines) and has a shape that does not resemble the substrate topography, such as in orb webs, cob webs, and canopy webs. This categorization followed the assumption that such aerial webs often have an increased demand in anchor robustness, because of the use of a limited number of anchor lines and higher exposure to mechanical impacts, such as wind, rain, and flying animals. Our phylogenetic analyses indicated that substrate webs are the ancestral state

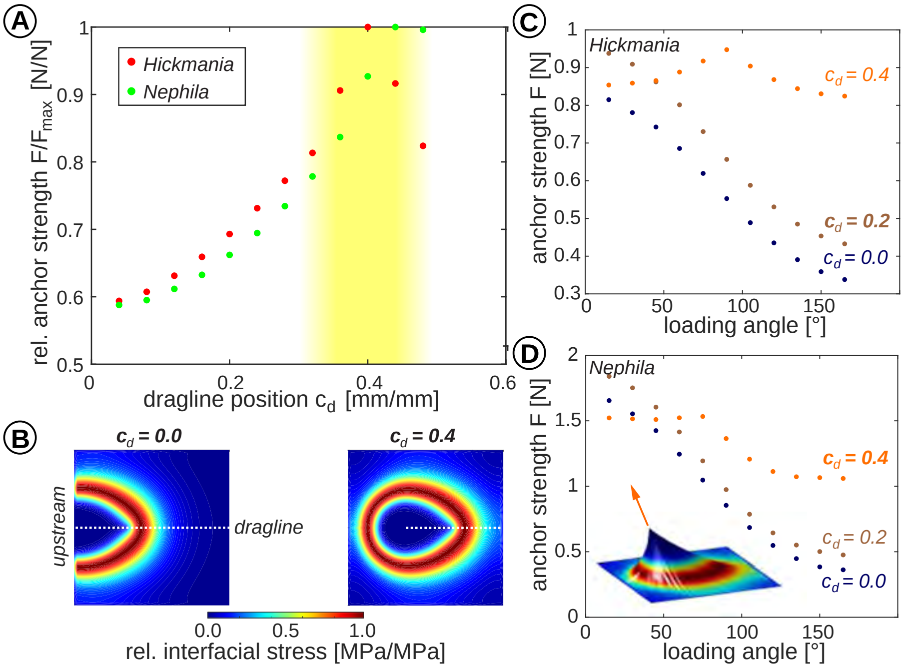

Figure 2. **Optimization of web anchor performance. (A) Simulated peak pull-off forces (anchor strength) versus different dragline positions for silk properties of Tasmanian cave spiders (*Hickmania troglodytes*) and golden orb weavers (*Nephila plumipes*) under vertical load. The yellow shade indicates the estimated range of c_d (for a variety of silk properties), where anchor strength is maximized. (B) Exemplary maps of interfacial stress in the silk membrane (apical view) for an orb weaver silk anchor with $c_d = 0.0$ and $c_d = 0.4$ under vertical load. Warm colors indicate high stress. Anchors reach the peak pull-off force when the interfacial stress concentration around the peeling line reaches the membrane edge. (C) Simulated anchor strength for different dragline loading angles between 15° (± parallel to substrate along spinning direction) and 165° (± parallel to substrate against spinning direction, i.e., dragline flipped over) and three different values of c_d (different colors, bold font indicates the mean c_d naturally found in this species) for silk properties of Tasmanian cave spiders. (D) Same as in (C) for silk properties of golden orb weavers. Inset shows three-dimensional displacement map and stress distribution in an anchor with $c_d = 0.4$, pulled at an angle of 75° (top-side view).**

in the Araneomorphae and aerial webs have evolved five to six times independently: at the basis of Araneoidea, in Uloboridae, Deinopidae, Pholcidae, and within Desidae (Fig. 3; Supporting Information 4).

We found, that lineages with anchors near the physical optimum of a dragline joint centrality $c_d = 0.3$–0.5 included all aerial web builders that lack a cribellum, one cribellate substrate web building species (*Megadictyna thilenii*), and some ecribellate hunting spiders belonging to Mimetidae, Arkyidae, Thomisidae, Oxyopidae, Trechaleidae, Philodromidae, Salticidae, and Toxopidae. We found multiple support for six shifts in the evolutionary regime of c_d (Fig. 3; Supporting Information 5): *shift 1* in Pholcidae (posterior probability $pp = 0.494$); *shift 2* in the grate-shaped tapetum clade (excluding Zoropsidae) ($pp = 0.474$); *shift 3* at the basis of Salticidae ($pp = 0.405$); *shift 4* at the basis of Entelegynae ($pp = 370$); *shift 5* at the basis of Araneoidea ($pp = 0.336$); and *shift 6* within Desidae (*Cambridgea*) ($pp = 0.309$). Shift 5 and 6 (both aerial web spinners; adaptive optimum $\theta \sim 0.36$ mm/mm), and shifts 1, 2, and 3 (aerial web spinning and hunting spiders; $\theta \sim 0.30$ mm/mm) were convergent, shifting toward similar evolutionary optima (Fig. 4F). Shifts 2, 5, and 6 coincided with cribellum loss and shifts 1 and 5 with the evolution of aerial webs. Notably all supported shifts led toward an elevated adaptive optimum θ. Our data suggest that the evolutionary trend toward an elevated c_d happened stepwise, for instance the exceptional c_d in Araneoidea evolved from an estimated root optimum of $\theta \sim 0.18$ mm/mm, with the first shift around 250 million years ago toward $\theta \sim 0.24$ mm/mm, and the second one around 180 million years ago toward $\theta \sim 0.36$ mm/mm. The exact location of these shifts differed between *SURFACE* and *bayou* methods, and an additional shift at the basis of Nicodamidoidea+Araneoidea around 200 million years ago is possible (Fig. 3; Supporting Information S5 and S6).

We found strong correlations between anchor structure and the configuration of the spinning apparatus. Spiders with a cribellum (the basal state) produced a significantly smaller dragline joint centrality c_d ($p = 0.005$; Supporting Information S7) and cribellum loss repeatedly led to an increase of c_d (Fig. 3). Furthermore, c_d correlated with spinning choreography, that is, the relative height of the spinneret trajectory geometry h_r ($P = 0.004$; Supporting Information S7): h_r is on average 1.6 times larger in

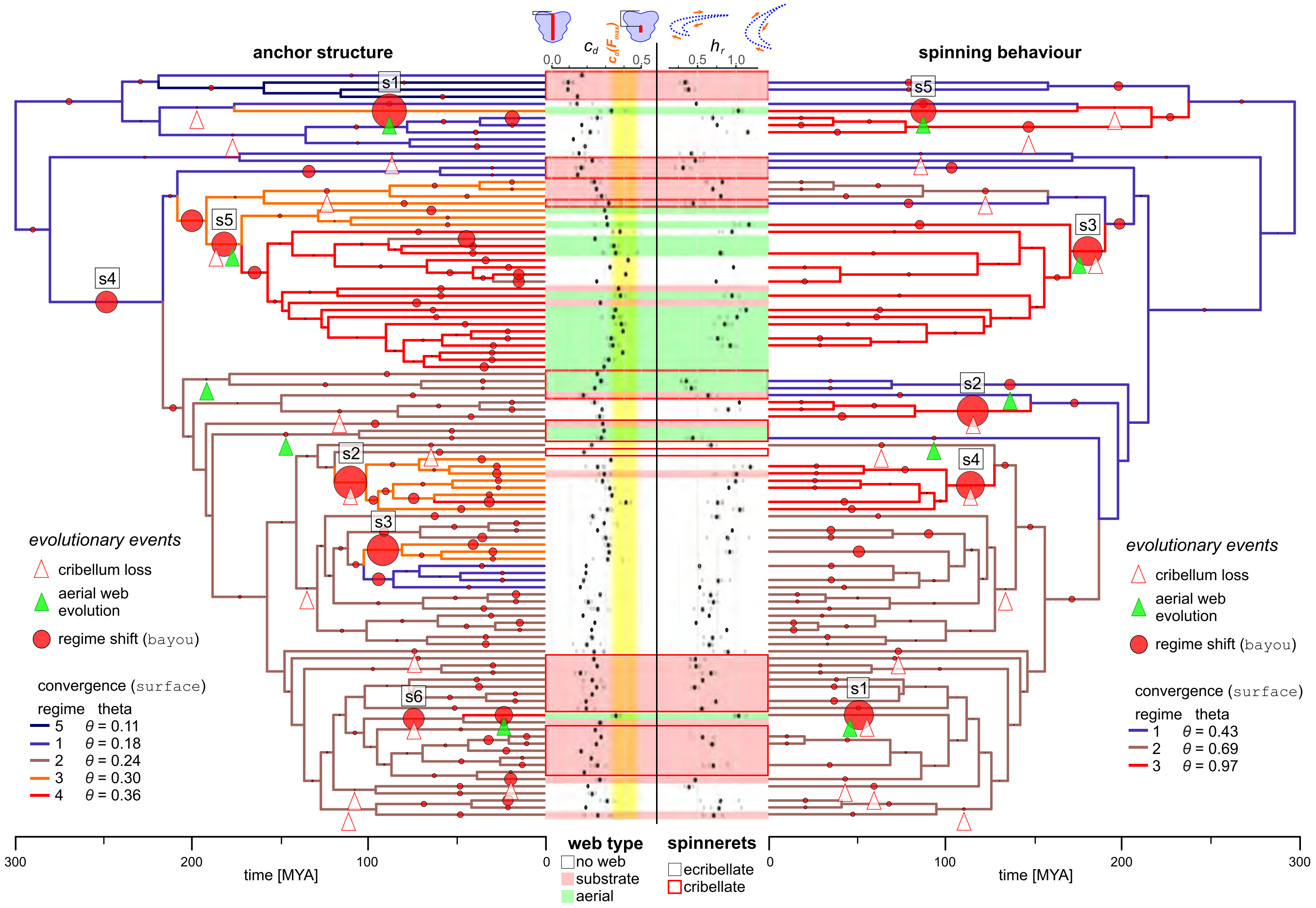

Figure 3. Correlated evolution of web structure, behavior, and morphology. Shifts in the adaptive landscape of dragline placement c_d (left tree) and spinning choreography h_r (right tree). Trees are displayed with the same terminals aligned, with the right tree being a sub-sample of the left tree. Branch colors denote convergent evolutionary regimes in the adaptive optimum θ as identified by *SURFACE*, with warmer colors indicating higher θs. The size of overlaid red pies indicates the posterior probability of a shift in θ in that branch, as found by *bayou*. Numbered shifts mark well supported shifts with $pp > 0.3$. White arrowheads with red outline indicate branches in which cribellum loss occurred, and green arrowheads indicate branches in which aerial web building has evolved (with a probability > 0.5). Dots at tips display c_d and h_r values measured in the extant species (grey dots represent means of individuals, black dot species means). The underlying shade indicates web building behaviour (white, no web; red, substrate web; green, aerial web) and the range of optimal anchor structure (yellow shade). Red boxes denote species with a cribellum. Schematics above symbolize anchors with a low and a high c_d (left; top view of anchor with membrane in blue and fused dragline in red) and spinning paths with a low and a high h_r (right; spinneret abducting to the right).

ecribellate spiders ($P < 0.001$; Supporting Information S7). These results were highly robust to phylogenetic uncertainty (Supporting Information S7). Notably, the shape of the spinning path did not differ between cribellate and ecribellate spiders ($P_r = 0.316$; Supporting Information S8). This indicates that it is not the shape of the spinning path, but its orientation and proportions that affect c_d. Our kinematic and morphological studies revealed that the cribellum mechanically constrains the mobility of the anchor producing spinnerets (the anterior lateral spinnerets) by blocking them on the anterior side. As a result, most cribellate spiders spread the spinnerets more laterally, leading to smaller h_r and c_d.

To further investigate if the configuration of the spinning apparatus (*c*) and web building behavior (*w*) had an effect on the evolutionary dynamics of c_d, we compared the fit of single and two-regime Brownian Motion (BM) and Ornstein–Uhlenbeck (OU) models. To account for phylogenetic uncertainty, we repeated the analyses across a sample of 100 phylogenetic trees.

We found strong support for a scenario, where the evolution of anchor structure was highly dynamic in substrate web builders and hunters, but stabilized around an elevated optimum in aerial web builders. Among all models, OUw models provided the best explanation for the extant variation of c_d (*AICcw* (OUMVAw) =

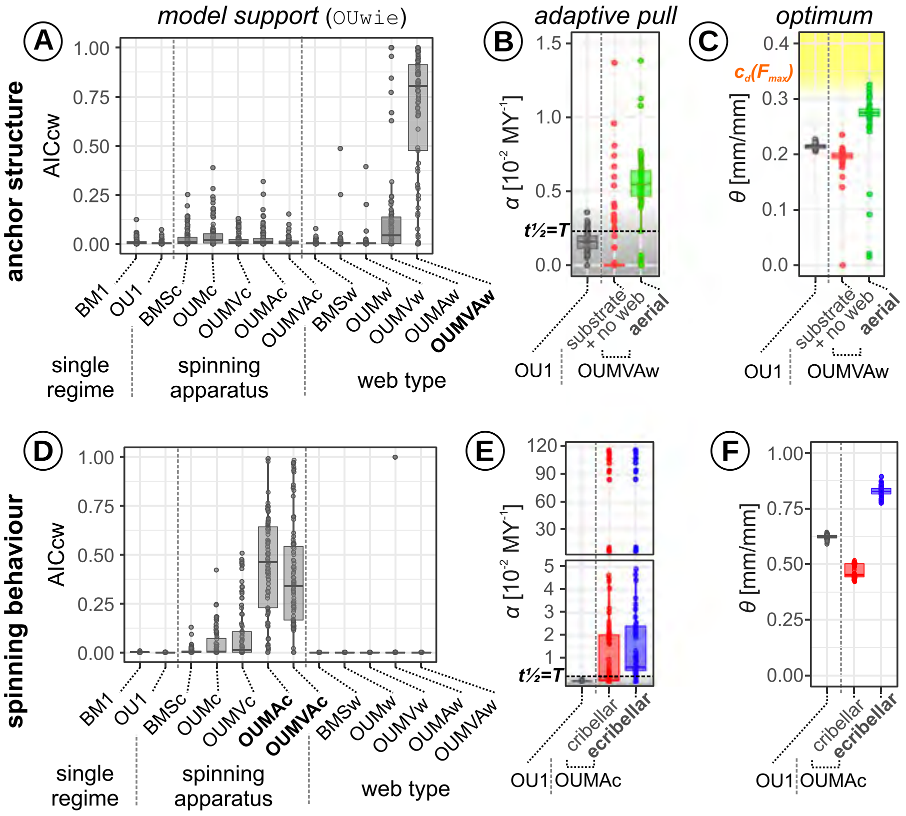

Figure 4. Heterogeneous evolution of anchor structure and spinning behavior. (A) *AICc*-weight values for single- and two-regime evolutionary models of dragline placement c_d across 100 trees (best supporting model in bold font). A clear support for OUMAw and OUMVAw indicates that c_d evolved towards an elevated optimum and at a higher adaptive potential (and higher evolutionary rates) in aerial web builders. (B) Summary of adaptive potential α of c_d for single regime OU-models ("null"-model), and the two regimes of the best fitting OUw model across 100 trees (some extreme outliers not displayed). The black dotted line indicates an α for which the phylogenetic half-life *t½* equals the total tree height *T*; below this threshold evolution becomes highly labile and BM-like (grey area). (C) Summary of the evolutionary optimum θ of c_d for single regime OU-models ("null"-model), and the two regimes of the best fitting OUw models across 100 trees. The yellow area indicates the theoretical physical optimum $c_d(F_{max})$. (D) Same as in (A) for spinning choreography h_r. A clear support for OUMAc and OUMVAc indicates that h_r evolved towards an elevated optimum and at a higher adaptive potential (and higher evolutionary rates) after cribellum loss. (E) Summary of adaptive potential α of h_r for single regime OU-models ('null'-model), and the two regimes of the best fitting OUc model across 100 trees. Same conventions as in (b). (F) Summary of the evolutionary optimum θ of h_r for single regime OU-models ("null"-model), and the two regimes of the best fitting OUc models across 100 trees. Same conventions as in (c).

0.667 ± 0.339; *AICcw* (OUMAw) = 0.163 ± 0.295; Fig. 4A). Under these models, c_d evolved at an increased adaptive optimum with a high adaptive potential in aerial web builders, while c_d of substrate web building and hunting spiders followed a stochastic evolution (i.e., *t½* >> *T*; Fig. 4B,C). There was support that cribellum loss affected the evolution of c_d (mean Δ*AICc* (OUMc-BM1) = 3.43, mean Δ*AICc* (OUMc-OU1) = 4.34). The best fit among OUc-models was the OUMc, a model under which c_d of ecribellate spiders had a higher adaptive optimum θ but evolutionary rates σ^2 and adaptive potential α did not differ between cribellate and ecribellate spiders. The inferred mean *t½* was close to the total height of the tree *T*, which represents a moderate α (Cooper et al. 2016).

Similar analyses on the spinning track proportions h_r indicated five shifts in the evolutionary regime (Fig. 3; Supporting Information S5). All but one shift coincided with cribellum loss, and three shifts co-occurred with aerial webs. Branches accommodating shifts 1, 3, 4, and 5 also had shifts in c_d, indicating a causal link. The constitution of the spinning apparatus had clearly affected the evolution of h_r (*AICcw*(OUMAc) = 0.442 ± 0.247; *AICcw*(OUMVAc) = 0.388 ± 0.269), whereas OUw models were indistinguishable from BM models (Fig. 4D). The contrasting results for c_d indicate that h_r alone does not explain c_d. There is, at least, one additional behavioral component affecting c_d, which is the movement of the body while a series of alternating spinneret movements are performed. The highest c_d values (excluding the hunting spider *Australomisidia*) were found in spiders that perform a back-and-forth movement of the abdomen during anchor production. This behavior has evolved independently in the Araneoidea and within the New Zealand Desidae.

Discussion

To our knowledge, this study is the first to assess attachment as a component in the evolution of animal architectures. We have shown that small changes in anchor structure profoundly affect web attachment. Notably, structural optimization does not necessarily come at a higher material cost, as the effect of dragline placement is significant for similar sized silk films. It therefore appears counter-intuitive that not all extant spiders exhibit an optimized anchor structure and that anchor building behavior evolved slowly and stepwise. Our results indicate this is due to two reasons.

First, the evolution of anchor structure is relaxed in substrate web builders and wandering spiders. Substrate web builders rely less on robust silk anchorages, because their webs are attached with numerous anchor lines and are usually less exposed to the environment than aerial webs. Hunting spiders may have different demands on silk anchorages, depending on whether draglines are used for locomotion, or whether silk is merely used in substrate-bound sheets for shelters and eggs sacs. This may explain the high variation and lability of c_d in hunting spiders.

Second, the evolution of anchor building behavior may be constrained by physical traits. Our data suggest that the cribellum organ, a sophisticated spinning plate that produces nanofiber-based capture threads, is one example of such a physical constraint on behavioral evolution. This is important since it provides an explanation for an old enigmatic problem in the understanding of spider web evolution: why nanofiber capture silk was lost so frequently across the spider tree (Miller et al. 2010a), resulting in cribellate spiders being largely outnumbered by ecribellate spiders (Bond and Opell 1998), and why only few cribellate spiders evolved aerial webs, although cribellate silk can be highly efficient in prey capture (Opell 1994; Opell and Schwend 2009; Bott et al. 2017). Our results indicate that the cribellum represents a significant physical constraint on the spinning of robust anchorages limiting the capability to build efficient suspended webs.

We found that all changes in the evolutionary mode of anchor spinning behavior followed or coincided with the loss of the cribellum. However, not all events of cribellum loss were followed by changes in the evolutionary dynamics of spinning behavior, indicating that further changes of physical traits, such as the arrangement of muscles and spinneret articulation, might have been necessary to alter spinning behavior in a way to optimize anchor structure. Cribellum loss may thus rather be an important precondition for further evolutionary enhancement of silk attachment.

Multiple support for an exceptional (i.e., faster and more stabilized) evolution of anchor structure in aerial web builders suggests its adaptive value for such webs. Aerial webs repeatedly evolved after or with evolutionary shifts in silk anchor structure and anchor spinning behavior occurred, supporting the idea that web anchor performance affects the evolution of web architecture.

Limited anchor performance may thus in itself be an important constraint in the evolution of web building behavior, and its improvement may have accelerated spider web diversification: web architecture is phylogenetically labile and enormously variable in ecribellate orb-web and cobweb spiders (Blackledge and Gillespie 2004; Eberhard et al. 2008; Kuntner et al. 2010), lineages in which anchor structure has reached the physical optimum. Such a rapid turnover of web building behavior may mask evolutionary histories in these lineages. Concluding that similarities in building routines indicate a common origin can be problematic in these cases, since the probability of parallelism is high (Ord and Summers 2015; York and Fernald 2017). Nevertheless, we note that the idea of an independent origin of orb webs in Araneoidea and Uloboridae as indicated by this and a previous study (Fernández et al. 2018) has recently received some scepticism (Garrison et al. 2016; Coddington et al. 2018; Eberhard 2018). In particular, it was argued that the loss of complex traits such as orb web building is more likely than their emergence, and the phylogenetic framework should account for that. Here, we tested three different evolutionary models, of which the ER model was statistically preferred. However, because our category “aerial web” contains different architectural shapes of webs, our results are not suited to draw definitive conclusions on the homology of a single architectural type, such as orbs—a question that is outside the scope of this study. Reconstructing the evolution of biomechanics and building routines of web elements other than anchors could help to resolve the chronology of evolutionary events that have preceded complex web architectures.

To the best of our knowledge, this is the first study that integrates physical and macro-evolutionary modeling to explain the evolution of animal architectures. Using web anchorages as an example, we demonstrate that to understand the evolution of complex behavior, like web building, it is essential to identify the interdependencies of behavioral and physical traits. Future works should therefore study the evolution of animal architectures and the morphology of their architects in combination.

We conclude that the evolution of behavior and extended phenotypes may not be as free as previously suggested (West-Eberhard 1989; Odling-Smee et al. 2003; Duckworth 2009; Bailey et al. 2018), but may rather be tightly bound to evolutionary changes in physical traits. In the case of spider webs the evolutionary removal of such physical constraints may have led to an evolutionary cascade resulting in an enormous diversity of web architectures and outstanding ecological success.

AUTHOR CONTRIBUTIONS

JOW devised, led, and administered the project. JOW, BRJ, AMR, and PM collected the data. MJR performed the phylogenetic inference. GBP, JOW, and AvdM performed the phylogenetic comparative analysis. NMP and FB developed and supervised, and DL carried out the physical numerical simulations. HS and MJR ensured taxonomic integrity. JOW, FB, and MEH wrote the manuscript. All authors critically revised the manuscript and approved its final version. MEH and NMP mentored the project.

ACKNOWLEDGMENTS

We are grateful to the following people, who assisted in the filming of spinning behavior, spider and silk sample collection, and spider maintenance, provided material and access to facilities, or helped with field trip logistics and spider identification: Mohammad Ameri, Arthur Clarke, Niall Doran, Jessica Garb, Arno Grabolle, Stanislav Gorb, Cristian Grismado, William Haynes, Siegfried Huber, Anna-Christin Joel, Alex Jordan, Lachlan Manning, Bryce McQuillan, Graham Milledge, Anna Namyatova, Ajay Narendra, Nicole O'Donnell, John Osmani, Robert Raven, Birte Schadlowski, Cristina Scioscia, Wolfgang Schlegel, Axel Schönhofer, Angela Simpson, Gabriele Uhl, Cor Vink, Zoe Wild, and Lydia Wolff. Some animals were collected under license SL101868 (Australia) and 64293-RES (New Zealand). This study was supported by a Macquarie Research Fellowship of Macquarie University and a Discovery Early Career Researcher Award of the Australian Research Council (DE190101338) to JOW. GBP was supported by a CAPES Doctoral Scholarship (PDSE: 88881.132040/2016-01). FB was supported by the FET Proactive "Neurofibres" grant no. 732344, the COST Action CA15216 "European Network of Bioadhesion Expertise," and by Progetto d'Ateneo/Fondazione San Paolo "Metapp," n. CSTO160004. NMP was supported by the European Commission H2020 under the Graphene Flagship Core 2 no. 785219 (WP14 "Composites") and the FET Proactive "Neurofibres" grant no. 732344, as well as by the Italian Ministry of Education, University and Research (MIUR) under the "Departments of Excellence" grant L.232/2016, the ARS01-01384-PROSCAN Grant and the PRIN-20177TTP3S Grant. MR was supported by the Agencia Nacional de Promoción Científica y Tecnológica, Argentina grant PICT-2015-0283. AvdM was supported by a grant by FCT under the Programa Operacional Potencial Humano – Quadro de Referência Estratégico Nacional funds from the European Social Fund and Portuguese Ministério da Educação e Ciência (SFRH/BPD/101057/2014). Computational resources were provided by the Centro di Competenza sul Calcolo Scientifico (C3S) of the University of Torino (c3s.unito.it).

COMPETING INTERESTS

The authors declare that they have no conflict of interests.

DATA ARCHIVING

Data matrices, trees and R code are archived online: https://doi.org/10.5281/zenodo.3374044. Additional details of statistical results are deposited in the Supporting Information.

LITERATURE CITED

Adams, D. C., and E. Otárola-Castillo. 2013. geomorph: an R package for the collection and analysis of geometric morphometric shape data. Methods Ecol. Evol. 4:393–399.

Alfaro, R. E., C. E. Griswold, and K. B. Miller. 2018. Comparative spigot ontogeny across the spider tree of life. PeerJ 6:e4233.

Bailey, N. W. 2012. Evolutionary models of extended phenotypes. Trends Ecol. Evol. 27:561–569.

Bailey, N. W., L. Marie-Orleach, and A. J. Moore. 2018. Indirect genetic effects in behavioral ecology: does behavior play a special role in evolution? Behav. Ecol. 29:1–11.

Beaulieu, J., and B. O'Meara. 2014. OUwie: analysis of evolutionary rates in an OU framework. R package version 1.5. Available at http://cran.r-project.org/web/packages/OUwie/index.html

Blackledge, T. A., and R. G. Gillespie. 2004. Convergent evolution of behavior in an adaptive radiation of Hawaiian web-building spiders. Proc. Natl. Acad. Sci. USA 101:16228–16233.

Blackledge, T. A., N. Scharff, J. A. Coddington, T. Szüts, J. W. Wenzel, C. Y. Hayashi, and I. Agnarsson. 2009. Reconstructing web evolution and spider diversification in the molecular era. Proc. Natl. Acad. Sci. USA 106:5229–5234.

Bond, J. E., N. L. Garrison, C. A. Hamilton, R. L. Godwin, M. Hedin, and I. Agnarsson. 2014. Phylogenomics resolves a spider backbone phylogeny and rejects a prevailing paradigm for orb web evolution. Curr. Biol. 24:1765–1771.

Bond, J. E., and B. D. Opell. 1998. Testing adaptive radiation and key innovation hypotheses in spiders. Evolution. 52:403–414.

Bott, R. A., W. Baumgartner, P. Bräunig, F. Menzel, and A. -C. Joel. 2017. Adhesion enhancement of cribellate capture threads by epicuticular waxes of the insect prey sheds new light on spider web evolution. Proc. R. Soc. B 284:20170363.

Bouckaert, R., J. Heled, D. Kühnert, T. Vaughan, C. -H. Wu, D. Xie, M. A. Suchard, A. Rambaut, and A. J. Drummond. 2014. BEAST 2: a software platform for Bayesian evolutionary analysis. PLoS Comput. Biol. 10:e1003537.

Brely, L., F. Bosia, and N. M. Pugno. 2015. A hierarchical lattice spring model to simulate the mechanics of 2-D materials-based composites. Front. Mater. 2:51.

Cheng, D. -Q., and W. H. Piel. 2018. The origins of the Psechridae: web-building lycosoid spiders. Mol. Phylogenet. Evol. 125:213–219.

Coddington, J. A. 1986. The monophyletic origin of the orb web. Pp. 319–363 *in* W. A. Shear, ed. Spiders. Webs, behavior, and evolution. Stanford Univ. Press, Stanford, CA.

Coddington, J. A. 2005. Phylogeny and classification of spiders. Pp. 18–24 *in* D. Ubick, P. Paquin, P. E. Cushing, and V. Roth, eds. Spiders of North America: an identification manual. American Arachnological Society, Berkeley, CA.

Coddington, J. A., I. Agnarsson, C. Hamilton, and J. E. J. P. P. Bond. 2018. Spiders did not repeatedly gain, but repeatedly lost, foraging webs. 6:e27341v27341.

Cook, R. D., D. S. Malkus, and M. E. Plesha. 2001. Concepts and applications of finite element analysis. John Wiley & Sons, Hoboken, NJ.

Cooper, N., G. H. Thomas, C. Venditti, A. Meade, and R. P. Freckleton. 2016. A cautionary note on the use of Ornstein Uhlenbeck models in macroevolutionary studies. Biol. J. Linn. Soc. 118:64–77.

Darriba, D., G. L. Taboada, R. Doallo, and D. Posada. 2012. jModelTest 2: more models, new heuristics and parallel computing. Nat. Methods 9:772.

Dawkins, R. 1982. The extended phenotype: the long reach of the gene. Oxford Univ. Press, Oxford, U.K.

Donoghue, M. J., and D. D. Ackerly. 1996. Phylogenetic uncertainties and sensitivity analyses in comparative biology. Phil. Trans. R. Soc. Lond. B 351:1241–1249.

Drummond, A. J., S. Y. Ho, M. J. Phillips, and A. Rambaut. 2006. Relaxed phylogenetics and dating with confidence. PLoS Biol. 4:e88.

Duckworth, R. A. 2009. The role of behavior in evolution: a search for mechanism. Evol. Ecol. 23:513–531.

Eberhard, W. G. 1990. Function and phylogeny of spider webs. Ann. Rev. Ecol. Syst. 21:341–372.

Eberhard, W. G. 2010. Possible functional significance of spigot placement on the spinnerets of spiders. J. Arachnol. 38:407–414.

Eberhard, W. G. 2018. Modular patterns in behavioural evolution: webs derived from orbs. Behaviour 155:531–566.

Eberhard, W. G., I. Agnarsson, and H. W. Levi. 2008. Web forms and the phylogeny of theridiid spiders (Araneae: Theridiidae): chaos from order. Syst. Biodivers. 6:415.

Felsenstein, J. 1985. Phylogenies and the comparative method. Am. Nat. 125:1–15.

Fernández, R., G. Hormiga, and G. Giribet. 2014. Phylogenomic analysis of spiders reveals nonmonophyly of orb weavers. Curr. Biol. 24:1772–1777.

Fernández, R., R. J. Kallal, D. Dimitrov, J. A. Ballesteros, M. A. Arnedo, G. Giribet, and G. Hormiga. 2018. Phylogenomics, diversification dynamics, and comparative transcriptomics across the spider tree of life. Curr. Biol. 28:1489–1497.

Freckleton, R. P., P. H. Harvey, and M. Pagel. 2002. Phylogenetic analysis and comparative data: a test and review of evidence. Am. Nat. 160:712–726.

Garrison, N. L., J. Rodriguez, I. Agnarsson, J. A. Coddington, C. E. Griswold, C. A. Hamilton, M. Hedin, K. M. Kocot, J. M. Ledford, and J. E. Bond. 2016. Spider phylogenomics: untangling the Spider Tree of Life. PeerJ 4:e1719.

Grafen, A. 1989. The phylogenetic regression. Phil. Trans. R. Soc. Lond. B 326:119–157.

Hansell, M. H. 2005. Animal architecture. Oxford Univ. Press, New York, NY.

Ho, L. S. T., and C. Ané. 2014. Intrinsic inference difficulties for trait evolution with Ornstein-Uhlenbeck models. Methods Ecol. Evol. 5:1133–1146.

Ingram, T., and D. L. Mahler. 2013. SURFACE: detecting convergent evolution from comparative data by fitting Ornstein-Uhlenbeck models with stepwise Akaike Information Criterion. Methods Ecol. Evol. 4:416–425.

Kallal, R. J., R. Fernández, G. Giribet, and G. Hormiga. 2018. A phylotranscriptomic backbone of the orb-weaving spider family Araneidae (Arachnida, Araneae) supported by multiple methodological approaches. Mol. Phylogenet. Evol. 126:129–140.

Katoh, K., J. Rozewicki, and K. D. Yamada. 2017. MAFFT online service: multiple sequence alignment, interactive sequence choice and visualization. Briefings in bioinformatics. bbx108.

Kovoor, J. 1987. Comparative structure and histochemistry of silk-producing organs in arachnids. Pp. 160–186. Ecophysiology of spiders. Springer, Berlin, Germany.

Kuntner, M., S. Kralj-Fišer, and M. Gregorič. 2010. Ladder webs in orb-web spiders: ontogenetic and evolutionary patterns in Nephilidae. Biol. J. Linn. Soc. 99:849–866.

Maddison, W. P., S. C. Evans, C. A. Hamilton, J. E. Bond, A. R. Lemmon, and E. M. Lemmon. 2017. A genome-wide phylogeny of jumping spiders (Araneae, Salticidae), using anchored hybrid enrichment. Zookeys 695:89–101.

Meijering, E., O. Dzyubachyk, and I. Smal. 2012. Methods for cell and particle tracking. Methods Enzymol. 504:183–200.

Miller, J. A., A. Carmichael, M. J. Ramírez, J. C. Spagna, C. R. Haddad, M. Řezáč, J. Johannesen, J. Král, X. -P. Wang, C. E. J. M. P. Griswold, and Evolution. 2010a. Phylogeny of entelegyne spiders: affinities of the family Penestomidae (NEW RANK), generic phylogeny of Eresidae, and asymmetric rates of change in spinning organ evolution (Araneae, Araneoidea, Entelegynae). Mol. Phylogenet. Evol. 55:786–804.

Miller, M. A., W. Pfeiffer, and T. Schwartz. 2010b. Creating the CIPRES Science Gateway for inference of large phylogenetic trees. Pp. 1–8. Gateway Computing Environments Workshop (GCE), 2010. IEEE.

Odling-Smee, F. J., H. Odling-Smee, K. N. Laland, M. W. Feldman, and F. Feldman. 2003. Niche construction: the neglected process in evolution. Princeton Univ. Press, Princeton, U.K.

Opell, B. 1994. The ability of spider cribellar prey capture thread to hold insects with different surface features. Funct. Ecol. 8:145–150.

Opell, B. D., and H. S. Schwend. 2009. Adhesive efficiency of spider prey capture threads. Zoology 112:16–26.

Ord, T. J., and T. C. Summers. 2015. Repeated evolution and the impact of evolutionary history on adaptation. BMC Evol. Biol. 15:137.

Ostoja-Starzewski, M. 2002. Lattice models in micromechanics. Appl. Mech. Rev. 55:35–60.

Ostrowski, A. M. 1973. The Newton–Raphson method. Pp. 53–55 *in* A. M. Ostrowski, ed. Pure applied mathematics. Third edition of solution of equations and systems of equations. Elsevier Amsterdam, the Netherlands.

Paterno, G. B., C. Penone, and G. D. Werner. 2018. sensiPhy: An r-package for sensitivity analysis in phylogenetic comparative methods. Methods Ecol. Evol. 9:1461–1467.

Pennell, M. W., J. M. Eastman, G. J. Slater, J. W. Brown, J. C. Uyeda, R. G. FitzJohn, M. E. Alfaro, and L. J. Harmon. 2014. geiger v2. 0: an expanded suite of methods for fitting macroevolutionary models to phylogenetic trees. Bioinformatics 30:2216–2218.

Piorkowski, D., S. Blamires, N. Doran, C. P. Liao, C. L. Wu, and I. M. Tso. 2018. Ontogenetic shift toward stronger, tougher silk of a web-building, cave-dwelling spider. J. Zool. 304:81–89.

Pugno, N. M. 2011. The theory of multiple peeling. Int J Fracture 171:185–193.

Pugno, N. M., S. W. Cranford, and M. J. Buehler. 2013. Synergetic material and structure optimization yields robust spider web anchorages. Small 9:2747–2756.

Revell, L. J. 2012. phytools: an R package for phylogenetic comparative biology (and other things). Methods Ecol. Evol. 3:217–223.

Sahni, V., J. Harris, T. A. Blackledge, and A. Dhinojwala. 2012. Cobweb-weaving spiders produce different attachment discs for locomotion and prey capture. Nat. Commun. 3:1106.

Salehani, M. K., Irani, N., Müser, M. H., & Nicola, L. 2018. Modelling coupled normal and tangential tractions in adhesive contacts. Tribology International 124:93–101. https://doi.org/10.1016/j.triboint.2018.03.022.

Schneider, C. A., W. S. Rasband, and K. W. Eliceiri. 2012. NIH Image to ImageJ: 25 years of image analysis. Nat. Methods 9:671–675.

Swanson, B., T. Blackledge, J. Beltrán, and C. Hayashi. 2006. Variation in the material properties of spider dragline silk across species. Appl. Phys. A 82:213–218.

Tung Ho, L. s., and C. Ané. 2014. A linear-time algorithm for Gaussian and non-Gaussian trait evolution models. Syst. Biol. 63:397–408.

Turner, J. S., and R. C. Soar. 2008. Beyond biomimicry: what termites can tell us about realizing the living building. *in* I. Wallis, L. Bilan, M. Smith, and A. S. Kaz, eds. Paper presented at First International Conference on Industrialized, Intelligent Construction, 14–16 May, Loughborough University, Loughborough, U.K.

Uyeda, J. C., and L. J. Harmon. 2014. A novel Bayesian method for inferring and interpreting the dynamics of adaptive landscapes from phylogenetic comparative data. Syst. Biol. 63:902–918.

Uyeda, J. C., R. Zenil-Ferguson, and M. W. Pennell. 2018. Rethinking phylogenetic comparative methods. Syst. Biol. 67:1091–1109.

Wcislo, W. T. 1989. Behavioral environments and evolutionary change. Ann. Rev. Ecol. Syst. 20:137–169.

West-Eberhard, M. J. 1989. Phenotypic plasticity and the origins of diversity. Annu. Rev. Ecol. Syst. 20:249–278.

Wheeler, W. C., J. A. Coddington, L. M. Crowley, D. Dimitrov, P. A. Goloboff, C. E. Griswold, G. Hormiga, L. Prendini, M. J. Ramírez, and P. Sierwald. 2017. The spider tree of life: phylogeny of Araneae based on target-gene analyses from an extensive taxon sampling. Cladistics 33:574–616.

Wirth, M., J. O. Wolff, E. Appel, and S. N. Gorb. 2019. Ultrastructure of spider thread anchorages. J. Morphol. 280:534–543.

Wolff, J. O. 2017. Structural effects of glue application in spiders—What can we learn from silk anchors? Pp. 63–80 *in* L. Xue, L. Heepe, and S. N. Gorb, eds. Bio-inspired structured adhesives. Springer Science+Business Media, Dordrecht, the Netherlands.

Wolff, J. O., I. Grawe, M. Wirth, A. Karstedt, and S. N. Gorb. 2015. Spider's super-glue: thread anchors are composite adhesives with synergistic hierarchical organization. Soft Matter 11:2394–2403.

Wolff, J. O., and M. E. Herberstein. 2017. 3D-printing spiders: back-and-forth glue application yields silk anchorages with high pull-off resistance under varying loading situations. J. R. Soc. Interface 14:20160783.

Wolff, J. O., A. van der Meijden, and M. E. Herberstein. 2017. Distinct spinning patterns gain differentiated loading tolerance of silk thread anchorages in spiders with different ecology. Proc. Roy. Soc. B-Biol. Sc. 284:20171124.

York, R. A., and R. D. Fernald. 2017. The Repeated Evolution of Behavior. Fron. Ecol. Evol. 4:143.

Associate Editor: S. Patek
Handling Editor: M. R. Servedio

Supporting Information

Additional supporting information may be found online in the Supporting Information section at the end of the article.

S1. Estimation of silk membrane stiffness.
S2. Comparing numerical model results of silk anchor efficiency with empirical data.
S3. Consensus tree.
S4. Ancestral character estimation
S5. Summary of SURFACE results.
S6. Summary of bayou results.
S7. Summary of PGLS results.
S8. Summary of geometric morphometrics results.
S9. Material list and sample sizes.
S10. Terminals mapping.
S11. Genbank identifiers.

ESM.1. Estimation of silk membrane stiffness

Methods

To estimate realistic parameters for our numerical model of silk anchor mechanics, we performed exemplary lateral stress tests of anchors that had been carefully delaminated from polypropylene sheets. Each 7-8 anchors of the basal substrate web builder *H. troglodytes*, the hunting spider *I. villosa* and the aerial web builder *N. plumipes* were glued with cyanacrylate adhesive onto a cardboard strip, such that the central dragline was oriented along the apical edge of the strip. Thereby the glue was spread across one lateral wing of the membrane up to the dragline such that the dragline was fixed (Fig. S.1.1a). The cardboard strip was mounted into the Instron 5542 tensile tester (Instron, Norwood, USA) with a clamp and the stage with an attached ULC-0.5N load cell (Interface, Inc., Scottsdale, AZ, USA) was slowly driven towards the free side of the silk membrane. The lateral edge of the membrane was then glued onto another piece of cardboard that was attached to the load cell, leaving a free membrane sample of 0.11-1.00 mm gauge length. The stage was moved slightly downwards to prevent a pre-stress of the silk membrane during adhesive curing. The sample was stretched at a rate of 0.01 mm/s until rupture. The process was monitored with a Basler Ace 640×480pix camera (Basler AG, Ahrensburg, Germany) equipped with an extension tube, 1.33× and 0.25× lenses (Navitar, Inc., Rochester, NY, USA) at 15 frames per second to record membrane strain and crack propagation. For each species four tests showed an even fraction of the membrane and were further analysed. To calculate stress, we estimated a cross-sectional area of the membrane $A = w \times t$, where w is the width of the sample and t its thickness. Here, t is given by the observed density of the spinning trajectory (as found in the kinematic analysis), which determines how many layers of piriform silk are applied, with each layer corresponding to the mean diameter of piriform fibres (0.5 µm (Wolff et al., 2015)). The Young's Modulus of the membrane was derived from the initial slope of the stress strain curve.

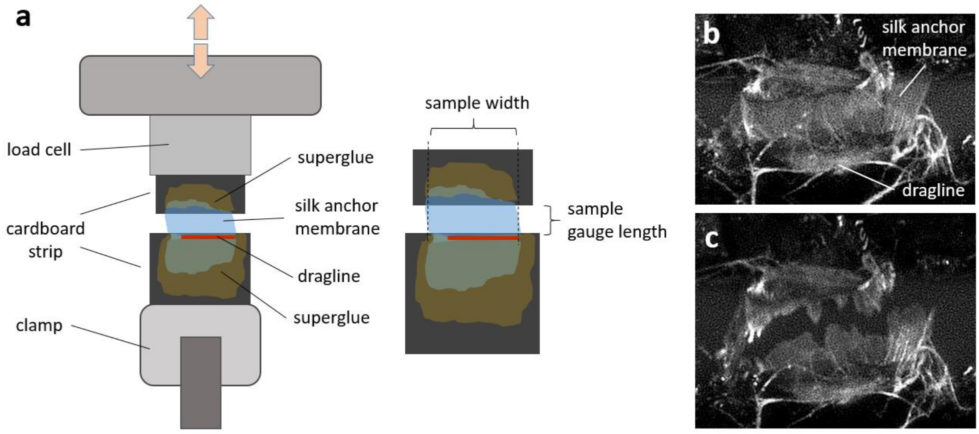

Fig. S1.1. (a) Schematic illustration of membrane stress tests to estimate membrane stiffness. (b) Video still of a stretched membrane of a *Nephila* silk anchor. (c) Similar silk membrane after rupture.

Results

Membranes of delaminated silk anchors generally had a 10-40 times lower stiffness than dragline silk of these or similar species (Piorkowski et al., 2018; Swanson et al., 2006). Silk membranes of *N. plumipes* were six times stiffer and stronger than the membranes of *I. villosa* and *H. troglodytes*, on average. This may be due to the grid-like overlay of fibres within the membrane (Wolff et al., 2015) caused by the specific back-and-forth spinning pattern in this spider.

Mechanical properties are summarized in Tab. S.1.1. below.

Tab. S1.1. Estimates of mechanical properties of silk anchor membranes from lateral stress tests.

Orb Weaver (*Nephila plumipes*)					
Sample no.	1	2	4	5	Mean ± s.d.
Length [mm]	0.33	0.31	0.67	0.25	
Width [mm]	1.93	1.17	1.29	1.28	
Extensibility [mm/mm]	0.05	0.11	0.53	0.33	0.26 ± 0.22
Strength [GPa]	0.149	0.214	0.168	0.319	0.212 ± 0.076
Young's Modulus [GPa]	3.02	2.28	0.25	1.17	**1.68** ± 1.22
Huntsman Spider (*Isopeda villosa*)					
Sample no.	3	4	7	8	Mean ± s.d.
Length [mm]	0.71	0.11	0.67	0.76	
Width [mm]	0.94	0.70	0.85	0.57	
Extensibility [mm/mm]	0.31	0.54	0.17	0.14	0.29 ± 0.18
Strength [GPa]	0.039	0.066	0.063	0.030	0.050 ± 0.018
Young's Modulus [GPa]	0.17	0.23	0.19	0.30	**0.22** ± 0.06
Tasmanian Cave Spider (*Hickmania troglodytes*)					
Sample no.	1	2	5	6	Mean ± s.d.
Length [mm]	1.00	0.32	0.66	0.16	
Width [mm]	1.35	0.50	1.00	0.81	
Extensibility [mm/mm]	0.19	0.33	0.14	0.32	0.25 ± 0.09
Strength [GPa]	0.016	0.075	0.023	0.028	0.035 ± 0.027
Young's Modulus [GPa]	0.29	0.27	0.34	0.09	**0.25** ± 0.11

For the numerical model of silk anchor mechanics, we used rounded numbers of the observed membrane and dragline stiffness parameters.

References

Piorkowski, D., Blamires, S., Doran, N., Liao, C. P., Wu, C. L. and Tso, I. M. (2018). Ontogenetic shift toward stronger, tougher silk of a web-building, cave-dwelling spider. *Journal of Zoology* **304**, 81-89.

Swanson, B., Blackledge, T., Beltrán, J. and Hayashi, C. (2006). Variation in the material properties of spider dragline silk across species. *Applied Physics A* **82**, 213-218.

Wolff, J. O., Grawe, I., Wirth, M., Karstedt, A. and Gorb, S. N. (2015). Spider's super-glue: thread anchors are composite adhesives with synergistic hierarchical organization. *Soft Matter* **11**, 2394-2403.

ESM.2. Comparing numerical model results of silk anchor efficiency with empirical data

Previous comparative measurements in silk anchors of orb weavers have revealed that centrality is the most (and only) significant variable of attachment disc structure that explains variation in maximal pull-off forces (Wolff & Herberstein, 2017). To derive a general relationship between centrality (front shift) and pull-off force, we used fracture mechanics theory to build a numerical model and simulated pull-off forces for different values of centrality (see main text). We found that the relationship resembles a curve, and pull-off force is maximized between $c_d = 0.3$ and $c_d = 0.5$.

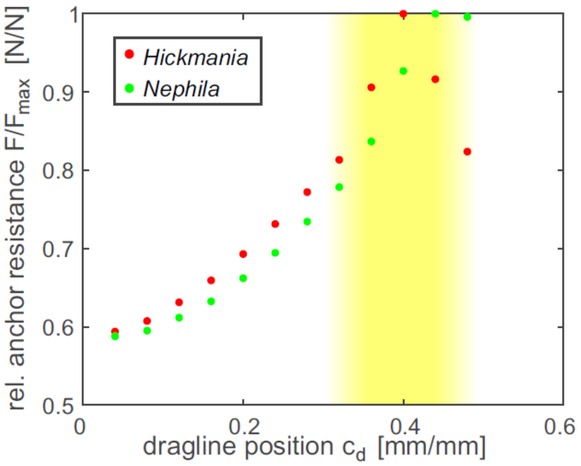

We re-analysed the data by Wolff and Herberstein (2017), and calculated c_d and F_{max}/A (maximal pull-off force normalized on projected anchor area).

We found that the relationship is consistent with the numerical results for *Nephila* anchors.

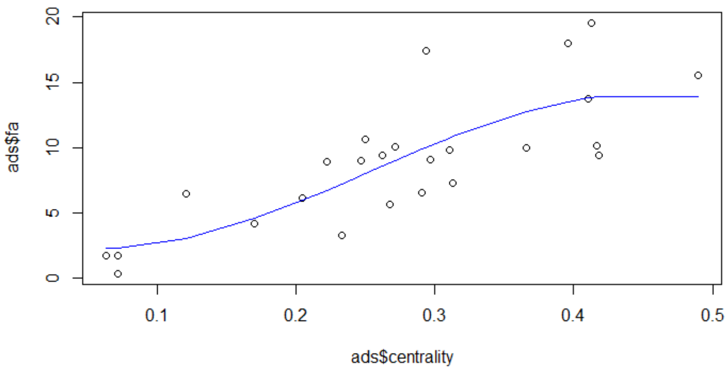

Fitting a sine curve:

```
Call:
lm(formula = ads$fa ~ xc + xs)

Residuals:
    Min      1Q  Median      3Q     Max 
-4.5118 -2.7686 -0.3529  1.5837  7.4274 

Coefficients:
            Estimate Std. Error t value Pr(>|t|)    
(Intercept)    8.205      1.315   6.238 2.81e-06 ***
xc            -5.418      1.205  -4.496  0.00018 ***
```

```
xs            -2.474      1.608  -1.538  0.13827
---
Signif. codes:  0 ‘***’ 0.001 ‘**’ 0.01 ‘*’ 0.05 ‘.’ 0.1 ‘ ’ 1

Residual standard error: 3.273 on 22 degrees of freedom
Multiple R-squared:  0.6137, Adjusted R-squared:  0.5786
F-statistic: 17.48 on 2 and 22 DF,  p-value: 2.856e-05
```

Fitting a linear model:

```
Call:
lm(formula = ads$fa ~ ads$centrality)

Residuals:
    Min      1Q  Median      3Q     Max
-4.4656 -2.0683 -0.3826  1.2083  7.8337

Coefficients:
               Estimate Std. Error t value Pr(>|t|)
(Intercept)     -0.4676     1.6497  -0.283    0.779
ads$centrality  34.2819     5.5467   6.181 2.64e-06 ***
---
Signif. codes:  0 ‘***’ 0.001 ‘**’ 0.01 ‘*’ 0.05 ‘.’ 0.1 ‘ ’ 1

Residual standard error: 3.157 on 23 degrees of freedom
Multiple R-squared:  0.6242, Adjusted R-squared:  0.6078
F-statistic:  38.2 on 1 and 23 DF,  p-value: 2.636e-06
```

References

Wolff, Jonas O., and Marie E. Herberstein. "Three-dimensional printing spiders: back-and-forth glue application yields silk anchorages with high pull-off resistance under varying loading situations." *Journal of The Royal Society Interface* 14.127 (2017): 20160783.


Liphistiidae_Liphistius
Antrodiaetidae_Antrodiaetus_unicolor
Hypochilidae_Hypochilus_pococki
Filistatidae_Pikelinia_tambilloi
Filistatidae_Filistata_insidiatrix
Filistatidae_Kukulcania_hibernalis
Pholcidae_Pholcus_phalangioides
Scytodidae_Scytodes_thoracica
Dysderidae_Harpactea_hombergi
Orsolobidae_Tasmanoonops_sp_MR690
Segestriidae_Ariadna_boesenbergi
Segestriidae_Gippsicola_sp
Segestriidae_Segestria_senoculata
Austrochilidae_Hickmania_troglodytes
Gradungulidae_Tarlina_woodwardi
Eresidae_Eresus_walckenaeri
Eresidae_Stegodyphus_lineatus
Megadictynidae_Megadictyna_thilenii
Nicodamidae_Dimidamus_dimidiatus
Nicodamidae_Litodamus_olga
Nicodamidae_Oncodamus_decipiens
Theridiidae_Episinus_antipodianus
Theridiidae_Cryptachaea_riparia
Theridiidae_Dipoena_cf_hortoni
Mimetidae_Australomimetus_sp_NS112
Tetragnathidae_Meta_sp_GH47
Tetragnathidae_Leucauge_venusta
Tetragnathidae_Tetragnatha_sp_GH19_GH27
Arkyidae_Arkys_curtulus
Arkyidae_Arkys_furcatus
Arkyidae_Arkys_cornutus
Arkyidae_Arkys_lancearius
Linyphiidae_Linyphia_triangularis
Pimoidae_Pimoa_altioculata
Physoglenidae_Tupua_sp_CG299
Araneidae_Phonognatha_graeffei
Araneidae_Nephila_pilipes
Araneidae_Eriophora_sp_GH7_GH21
Araneidae_Arachnura_logio
Araneidae_Gasteracantha_cancriformis
Araneidae_Poecilopachys_australasia
Araneidae_Argiope_bruenicchi
Araneidae_Cyrtophora_citricola
Araneidae_Cyrtophora_moluccensis
Uloboridae_Waitkera_waitakerensis
Uloboridae_Philoponella_congregabilis
Uloboridae_Philoponella_variabilis
Oecobiidae_Oecobius_sp_TAB2009
Hersiliidae_Hersilia_sericea
Hersiliidae_Tamopsis_sp2
Hersiliidae_Tamopsis_sp3
Titanoecidae_Goeldia_sp_MR17
Deinopidae_Deinopis_spinosa
Deinopidae_Menneus_camelus
Sparassidae_Isopeda_parnabyi
Amaurobiidae_Amaurobius_fenestralis
Dictynidae_Brigittea_latens
Dictynidae_Paradictyna_rufoflava
Agelenidae_Tegenaria_domestica
Toxopidae_Toxops_sp_CG278
Toxopidae_Toxopsoides_sp
Cycloctenidae_Cycloctenus_sp_CG98
Cycloctenidae_Pakeha_sp_CG169
Stiphidiidae_Neolana_sp_CG121
Stiphidiidae_Taurongia_sp
Stiphidiidae_Therlinya_sp_CG297
Stiphidiidae_Stiphidion_sp
Stiphidiidae_Stiphidion_sp_CG91
Desidae_Cambridgea_plagiata
Desidae_Cambridgea_sp_CG97
Desidae_Barahna_sp_CG293
Desidae_Austmusia_wilsoni
Desidae_Metaltella_sp_CG60
Desidae_Badumna_insignis
Desidae_Badumna_longinqua
Desidae_Forsterina_sp
Desidae_Matachiinae_spec
Desidae_Paramatachia_sp_CG277
Zoropsidae_Kilyana_hendersoni
Zoropsidae_Zoropsis_spinimana
Trechaleidae_Trechalea_bucculenta
Pisauridae_Dendrolycosa_cruciata
Pisauridae_Dolomedes_sp_CG96
Oxyopidae_Oxyopes_salticus
Thomisidae_Australomisidia_pilula
Thomisidae_Tharpina_campestrata
Thomisidae_Sidymella_angulata
Thomisidae_Stephanopis_cambridgei
Anyphaenidae_Amaurobioides_maritima
Anyphaenidae_Anyphaena_accentuata
Clubionidae_Clubiona_sp1
Clubionidae_Clubiona_huttoni
Clubionidae_Clubiona_sp2
Eutichuridae_Calamoneta_sp_MR661
Corinnidae_Leichhardteus_albofasciatus
Corinnidae_Nyssus_albomaculatus
Corinnidae_Nyssus_cf_coloripes
Philodromidae_Philodromus_aureolus
Philodromidae_Tibellus_chamberlini
Philodromidae_Tibellus_oblongus
Salticidae_Servaea_incana
Salticidae_Opisthoncus_kochi
Salticidae_Sandalodes_bipenicillatus
Miturgidae_Argoctenus_sp_CG26
Miturgidae_Nuliodon_fishburni
Miturgidae_Mituliodon_tarantulinus
Miturgidae_Miturga_lineata
0.36
0.3
0.68
0.27
0.89
0.87
0.6
0.98
0.72
0.95
0.99
0.57
0.49
0.63
0.57
0.68
0.36
0.69
0.82
0.89
0.99
0.35
0.5
0.99
0.94
0.47
-400
-300
-200
-100
0

ESM.4. Ancestral Character Estimation of web type

Model comparison (AICc weights)

```
       ER       SYM       ARD 
0.5825985 0.1818513 0.2355502 
```

Stochastic Character Mapping

ER

100 times on consensus tree

```
make.simmap is sampling character histories conditioned on the transition matrix

Q =
             0            1            2
0 -0.002082653  0.001041326  0.001041326
1  0.001041326 -0.002082653  0.001041326
2  0.001041326  0.001041326 -0.002082653
(estimated using likelihood);
and (mean) root node prior probabilities
pi =
        0         1         2 
0.3333333 0.3333333 0.3333333 

100 trees with a mapped discrete character with states:
 0, 1, 2 

trees have 25.19 changes between states on average

changes are of the following types:
      0,1  0,2  1,0  1,2  2,0  2,1
x->y 2.81 1.49 8.13 5.72 3.98 3.06

mean total time spent in each state is:
             0            1            2    total
raw  4172.6046685 5053.3308585 2790.3464610 12016.28
prop    0.3472459    0.4205403    0.2322138     1.00
```

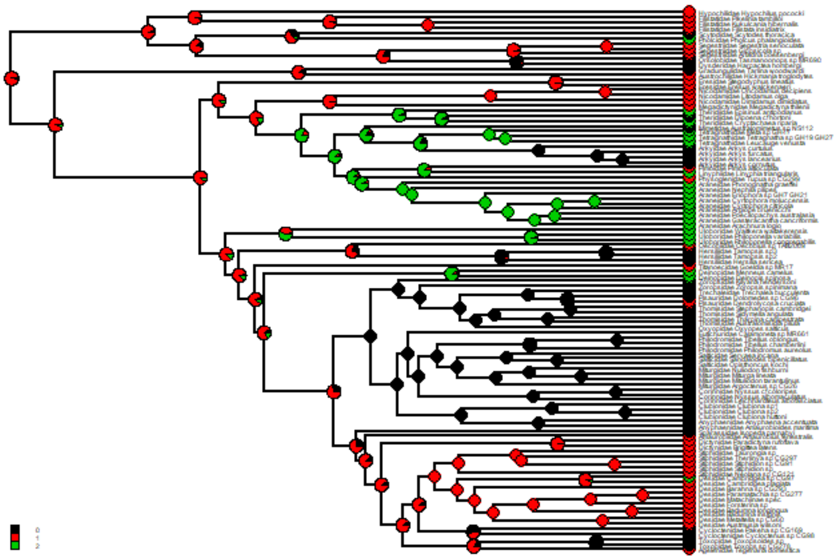

Including phylogenetic uncertainty (across 100 trees)

```
100 trees with a mapped discrete character with states:
 0, 1, 2

trees have 26.5 changes between states on average

changes are of the following types:
      0,1 0,2  1,0  1,2  2,0  2,1
x->y 3.24 1.6 7.92 5.96 4.51 3.27

mean total time spent in each state is:
                0            1            2    total
raw  4158.8882447 4922.7032452 2813.0397605 11894.63
prop    0.3493514    0.4140903    0.2365583     1.00
```

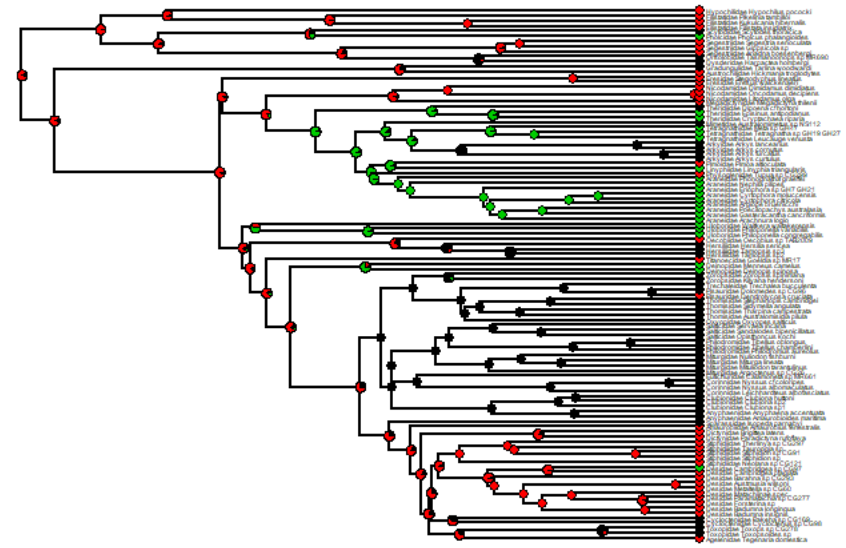

ARD

100 times on consensus tree

```
make.simmap is sampling character histories conditioned on the transition matrix

Q =
              0             1            2
0 -0.0004125627  0.0004125627  0.000000000
1  0.0016196521 -0.0029227069  0.001303055
2  0.0012480697  0.0010154840 -0.002263554
(estimated using likelihood);
and (mean) root node prior probabilities
pi =
        0         1         2
0.3333333 0.3333333 0.3333333

100 trees with a mapped discrete character with states:
 0, 1, 2

trees have 23.28 changes between states on average

changes are of the following types:
      0,1 0,2  1,0  1,2  2,0  2,1
x->y 1.58   0 8.61 6.71 3.46 2.92

mean total time spent in each state is:
               0            1            2    total
raw  3945.137882 5263.4162177 2807.7278887 12016.28
prop    0.328316    0.4380237    0.2336603     1.00
```

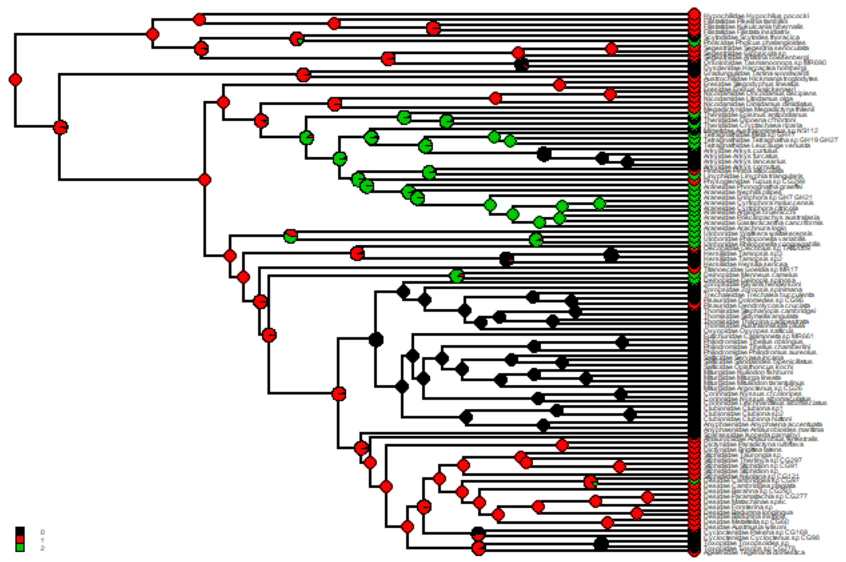

Ancestral Character Estimation of spinning apparatus state

Model comparison (AICc weights)

```
        ER        ARD      Dollo
0.00201729 0.35779483 0.64018788
```

Stochastic Character Mapping

Dollo's Law

100 times on consensus tree

```
make.simmap is sampling character histories conditioned on the transition matrix

Q =
            0            1
0 0.000000000  0.000000000
1 0.003021743 -0.003021743
(estimated using likelihood);
and (mean) root node prior probabilities
pi =
  0   1
0.5 0.5


100 trees with a mapped discrete character with states:
 0, 1

trees have 15.28 changes between states on average

changes are of the following types:
     0,1   1,0
x->y   0 15.28

mean total time spent in each state is:
             0            1    total
raw  6932.4776368 5083.8043512 12016.28
prop    0.5769237    0.4230763     1.00
```

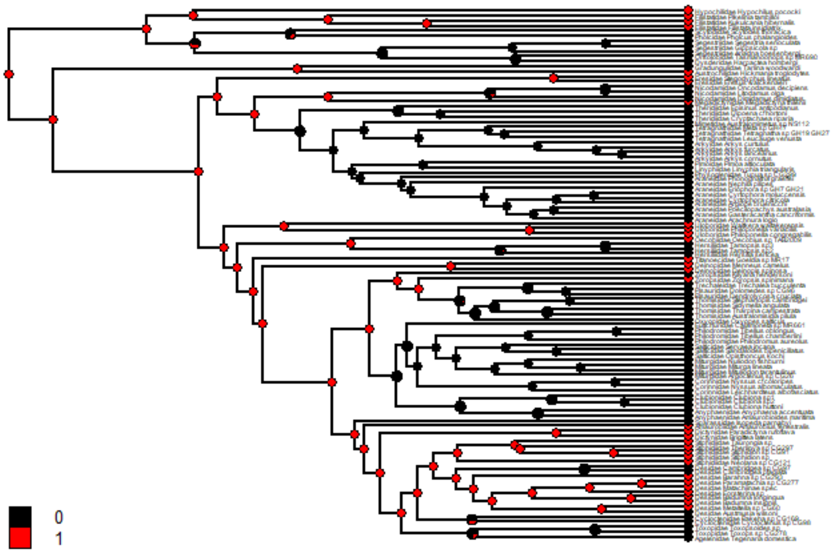

Including phylogenetic uncertainty (across 100 trees)

```
100 trees with a mapped discrete character with states:
 0, 1

trees have 16.26 changes between states on average

changes are of the following types:
     0,1   1,0
x->y   0 16.26

mean total time spent in each state is:
                0            1    total
raw  6792.9713724 5101.6598780 11894.63
prop    0.5708267    0.4291733     1.00
```

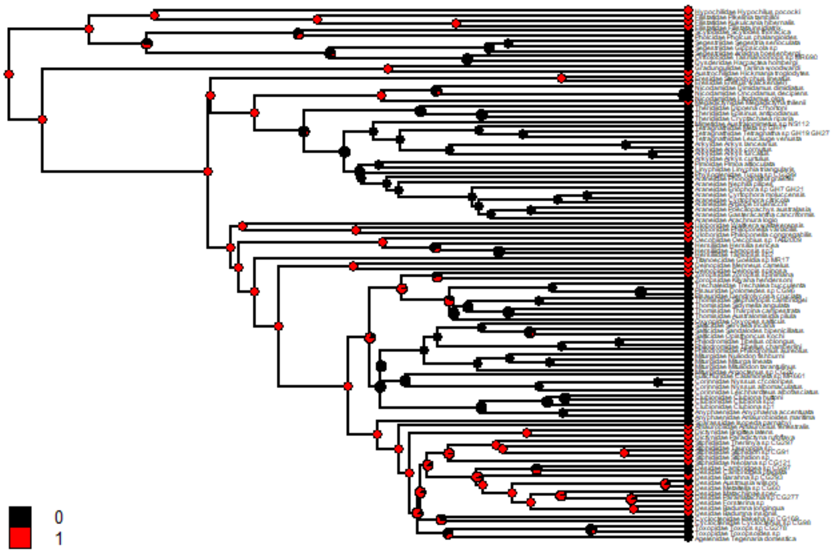

ESM.5. *Summary of SURFACE results.*

Centrality

```
> surfaceSummary(centrSurf$fwd, centrSurf$bwd)
$`n_steps`
[1] 19

$lnls
               [,1]     [,2]     [,3]     [,4]     [,5]     [,6]     [,7]     [,8]     [,9]
[,10]    [,11]    [,12]
centrality 148.9926 154.8584 160.7192 167.1772 173.0176 177.6523 182.3514 186.6792 190.2654 1
94.0089 197.7598 201.7447
              [,13]   [,14]    [,15]    [,16]    [,17]    [,18]    [,19]
centrality 205.9621 205.962 205.9537 205.9372 205.8607 205.7536 203.1835

$n_regimes_seq
               [,1] [,2] [,3] [,4] [,5] [,6] [,7] [,8] [,9] [,10] [,11] [,12] [,13] [,14] [,1
5] [,16] [,17] [,18] [,19]
k                 1    2    3    4    5    6    7    8    9    10    11    12    13    13
13    13    13    13    13
kprime            1    2    3    4    5    6    7    8    9    10    11    12    13    12
11    10     9     8     5
deltak            0    0    0    0    0    0    0    0    0     0     0     0     0     1
2     3     4     5     8
c                 0    0    0    0    0    0    0    0    0     0     0     0     0     2
4     6     7     9    12
kprime_conv       0    0    0    0    0    0    0    0    0     0     0     0     0     1
2     3     3     4     4
kprime_nonconv    1    2    3    4    5    6    7    8    9    10    11    12    13    11
9     7     6     4     1

$aics
        1         2         3         4         5         6         7         8         9
10        11        12
-289.5851 -296.8597 -303.9383 -312.0140 -318.6439 -322.6380 -326.5211 -329.4050 -330.5309 -33
1.6764 -332.5195 -333.4894
       13        14        15        16        17        18        19
-334.5558 -338.2875 -341.9074 -345.4187 -348.7215 -351.8776 -356.3670

$shifts
  1  39 102  53 110  37  59 195  62 128 134   3 165
"a" "b" "c" "b" "b" "f" "b" "f" "a" "c" "c" "l" "f"

$n_regimes
             k         kprime         deltak              c    kprime_conv kprime_nonconv
            13              5              8             12              4              1

$alpha
centrality
  1.746556

$phylhalflife
centrality
 0.3968652

$sigma_squared
 centrality
0.004265715

$theta
  centrality
a  0.1786923
b  0.2996083
c  0.2377853
f  0.3591632
l  0.1113329
```

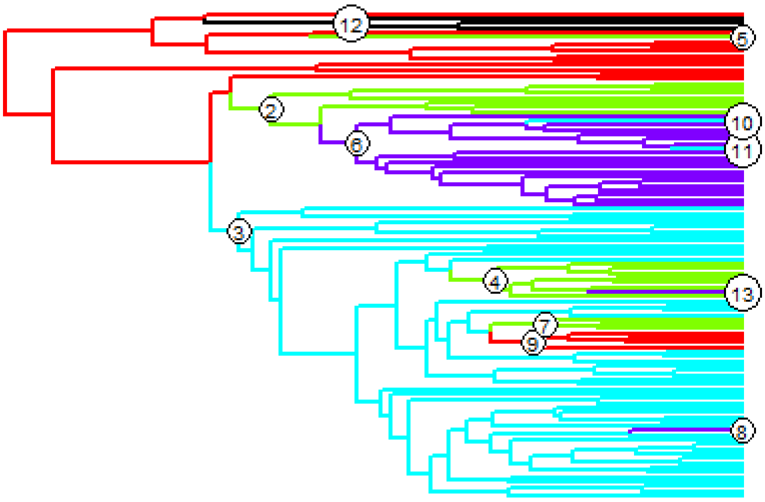

Spinning track proportions

```
> surfaceSummary(trackSurf$fwd, trackSurf$bwd)
$`n_steps`
[1] 11

$lnls
                   [,1]     [,2]     [,3]     [,4]    [,5]     [,6]    [,7]     [,8]     [,9]
[,10]    [,11]
smu_rel_height 9.751597 13.44973 17.18656 21.45115 24.6963 29.28001 35.3672 39.12883 39.08978
37.9916 37.35386

$n_regimes_seq
               [,1] [,2] [,3] [,4] [,5] [,6] [,7] [,8] [,9] [,10] [,11]
k                 1    2    3    4    5    6    7    8    8     8     8
kprime            1    2    3    4    5    6    7    8    7     4     3
deltak            0    0    0    0    0    0    0    0    1     4     5
c                 0    0    0    0    0    0    0    0    2     6     8
kprime_conv       0    0    0    0    0    0    0    0    1     2     3
kprime_nonconv    1    2    3    4    5    6    7    8    6     2     0

$aics
        1         2         3         4         5         6         7         8         9
10        11
-10.89713 -13.58695 -16.05053 -19.23564 -20.01329 -23.06002 -28.66033 -29.10381 -32.63240 -40
.48321 -42.32176

$shifts
  1  21  26  32   6  65  10  73
"a" "b" "b" "b" "b" "f" "f" "a"

$n_regimes
             k         kprime         deltak              c    kprime_conv kprime_nonconv
             8              3              5              8              3              0

$alpha
smu_rel_height
      0.351283

$phylhalflife
smu_rel_height
      1.973187

$sigma_squared
smu_rel_height
    0.01436403

$theta
  smu_rel_height
a      0.4272920
b      0.9686941
f      0.6853987
```

<u>ESM.6</u>. Summary of results from *Bayou*-Analysis

<u>Centrality</u>

We found multiple support for six shifts in the evolutionary regime of c_d (*pp* means for all chains with a prior of 20 and 25 shifts given): *shift 1* in Pholcidae (posterior probability *pp* = 0.494); *shift 2* in the grate-shaped tapetum clade (excl. Zoropsidae) (*pp* = 0.474); *shift 3* at the basis of Salticidae (*pp* = 0.405); *shift 4* at the basis of Entelegynae (*pp* = 370); *shift 5* at the basis of Araneoidea (*pp* = 0.336); and *shift 6* within Desidae (*Cambridgea*) (*pp* = 0.309).
A graphical summary of the results from all MCMC chains are given below. Please note that chains with priors of 20 and 25 shifts arrived at a similar posterior and results in the main text are reported from these chains only.

dk=10

1st run

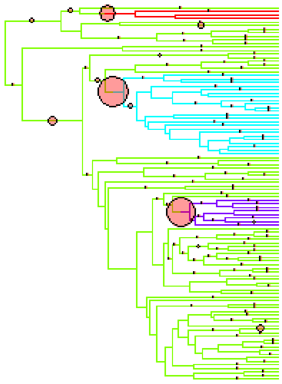

2nd run

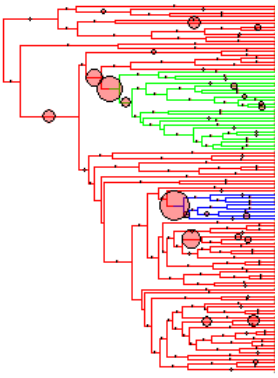

dk=15

1st run

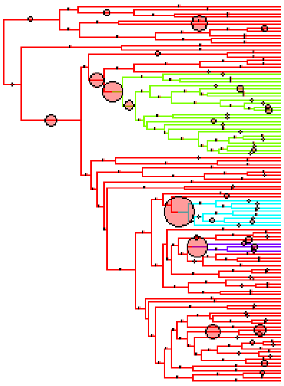

2nd run

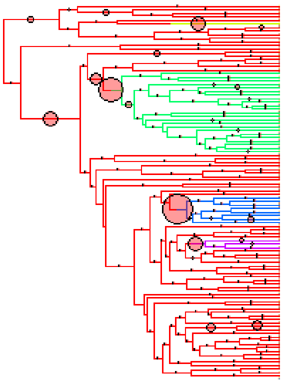

dk=20

1st run

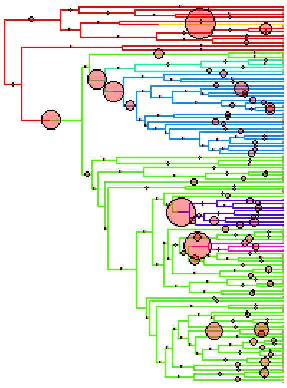

2nd run

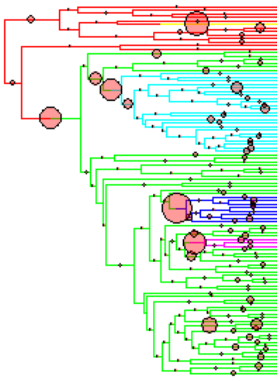

dk=25

1st run

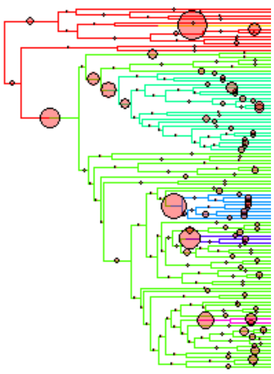

2nd run

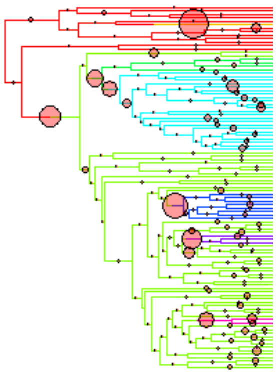

Track proportions

Analyses on the spinning track proportions h_r indicated five shifts in the evolutionary regime (*pp* means for all chains with a prior of 15, 20 and 25 shifts given): *shift 1* within Desidae (*Cambridgea*) (*pp* = 0.507); *shift 2* at the basis of Hersiliidae (*pp* = 0.584); *shift 3* at the basis of Araneoidea (*pp* = 0.579); *shift 4* in the grate-shaped tapetum clade (excl. Zoropsidae) (*pp* = 0.590); and shift 5 in Pholcidae (*pp* = 0.470) (Fig. 2).

A graphical summary of the results from all MCMC chains are given below. Please note that chains with priors of 15, 20 and 25 shifts arrived at a similar posterior and results in the main text are reported from these chains only.

dk=10

1st run

2nd run

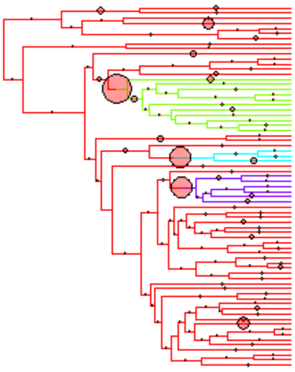

dk=15

1st run

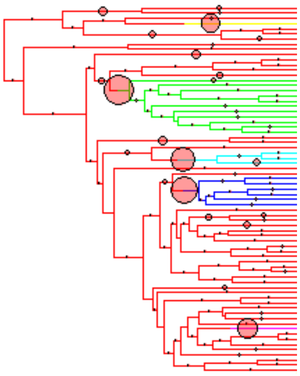

2nd run

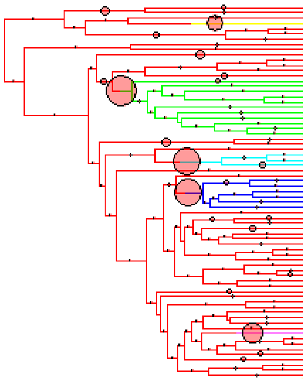

dk=20

1st run

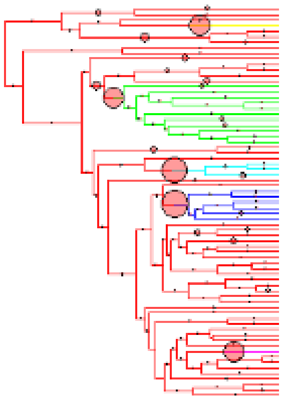

2nd run

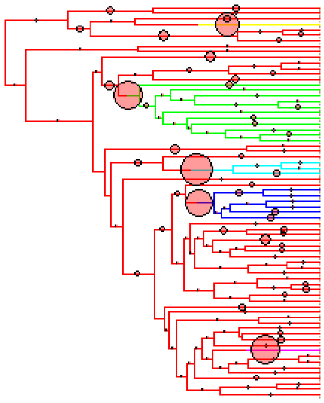

dk=25

1st run

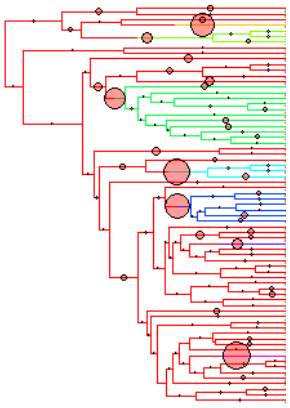

2nd run

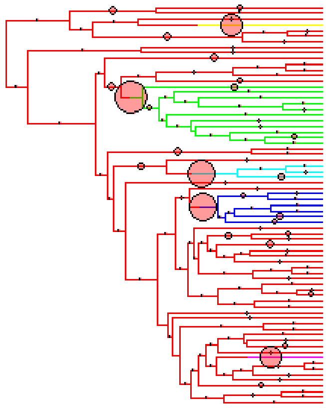

<u>ESM.7</u>. Phylogenetic Generalized Linear Squares analysis

Results from PGLS models demonstrate that spinning apparatus and web type correlate with silk anchor characteristics. For spinning apparatus, we found that cribellar species build anchors with lower dragline insertion location c_d (P = 0.0046) and track proportion h_r (P < 0.0001) in comparison to species without cribellum (Fig. S6.1a,d, Tab. S6.1). Results were less consistent for web type. Aerial web builders show a higher c_d than species that build substrate webs or no webs (Fig. S6.1d, Tab. S6.2). Besides the tendency of aerial web builders to show higher h_r, this effect was not statistically significant (Fig. S6.1a, Tab. S6.2). Results from phylogenetic regressions demonstrate a clear positive relationship between c_d and h_r (B = 0.113, P < 0.00001) (Fig. S6.1b, Tab. S6.3). All results from PGLS models were highly robust to phylogenetic uncertainty (see below).

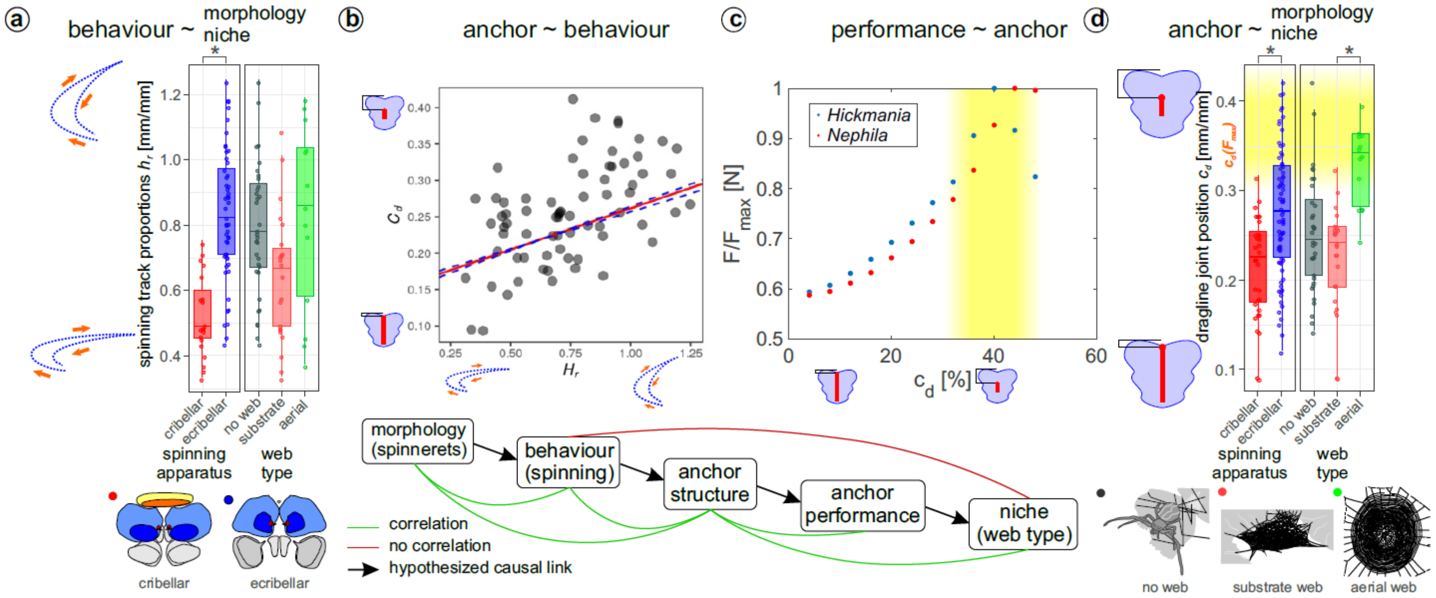

Fig. S6.1. Correlation of morphology, behaviour, biomechanics and ecology. ***(a)*** Data representation of spinning track proportions h_r. Asterisks above boxplots indicate significant difference between groups. Schematics left of the plot indicate a single movement unit of an anterior lateral spinneret during anchor production, with the arrows indicating the direction of movement (abducting to the right). Below plots a schematic illustration of the spinning apparatus in an exemplary cribellar (*Deinopis*) and ecribellar (*Argiope*) spider, with the cribellum (or the its inactive remnant, called colulus) in yellow (spinning field orange), the anterior lateral spinnerets in blue (darker hue for spinning fields) and the dragline spigot(s) in red. ***(b)*** Phylogenetic least square regression of web anchor structure (C_d) against geometric spinning trajectory proportions (H_r). The solid red line shows the average PGLS regression line (mean intercept and slope across 100 phylogenetic trees). Dashed blue lines represent phylogenetic uncertainty for the slope and intercept (minimum and maximum intercept and slope across 100 phylogenetic trees). See Tab. S6.3 for details. ***(c)*** Relationship between anchor resistance and web anchor structure, studied by numerical modeling (see main manuscript). ***(d)*** Data representation of web anchor structure c_d. Asterisks above boxplots indicate significant difference between groups. The yellow hue indicates the range of optimal c_d. Left of the plot a schematic illustration of anchor structure with the blue shape indicating the piriform silk film, the red line the fused dragline and the red pie the loading point (where the upstream dragline is inserted into the anchor). Schematic drawings under the plot illustrate exemplary silk uses in web type groups. Below plots (b) and (c) a summary of tested correlations and hypothesized causal links.

Tab. S6.1. Results from phylogenetic least square models (PGLS) for web anchor structure (c_d) and geometric spinning trajectory proportions (h_r) against spinning apparatus (cribellum). Estimates accounting for phylogenetic uncertainty are provided (average Beta, minimum, maximum and 95% confidence intervals of each parameter across 100 phylogenetic trees). Numbers in bold indicate significant effects (average $P < 0.05$).

c_d								
Variable	**Beta**	**min**	**max**	SD_{tree}	CI_{low}	CI_{high}	P	SD_P
Spinning apparatus	-0.045	-0.049	-0.041	0.002	-0.045	-0.044	**0.00461**	0.00158
h_r								
Spinning apparatus	-0.276	-0.299	-0.254	0.001	-0.278	-0.274	**0.00000**	0.00000

Tab. S6.2. Results from phylogenetic least square models (PGLS) for web anchor structure (c_d) and geometric spinning trajectory proportions (h_r) against web type (absent, substrate, aerial). Estimates accounting for phylogenetic uncertainty are provided (average Beta, minimum, maximum and 95% confidence intervals of each parameter across 100 phylogenetic trees). Numbers in bold indicate significant effects (average $P < 0.05$).

c_d								
Variable	**Beta**	**min**	**max**	SD_{tree}	CI_{low}	CI_{high}	P	SD_P
Intercept (Absent)	0.217	0.210	0.224	0.003	0.216	0.217	**0.00000**	0.00000
Substrate	-0.017	-0.021	-0.011	0.002	-0.017	-0.016	0.30053	0.05447
Aerial	0.041	0.036	0.049	0.002	0.041	0.042	**0.03553**	0.00921
h_r								
Intercept (Absent)	0.701	0.667	0.728	0.012	0.699	0.704	**0.00000**	0.00000
Substrate	-0.120	-0.144	-0.091	0.012	-0.123	-0.118	0.09858	0.03796
Aerial	0.020	-0.040	0.059	0.017	0.016	0.023	0.80425	0.11855

Tab. S6.3. Results from phylogenetic least square regressions for web anchor structure (c_d) against geometric spinning trajectory proportions (h_r). Regression estimates accounting for phylogenetic uncertainty are provided (average estimate, minimum, maximum and 95% confidence intervals for each parameter across 100 phylogenetic trees). SD_{tree} represents the standard deviation of estimates across trees. P represents the average P-value across all trees. SD_P is the standard deviation in P-values across trees. Numbers in bold indicate significant effects (average $P < 0.05$).

$c_d \sim h_r$								
Parameter	**Estimate**	**min**	**max**	SD_{tree}	CI_{low}	CI_{high}	P	SD_P
Intercept	0.148	0.142	0.155	0.003	0.148	0.149	**0.00000**	0.00000
Slope	0.113	0.102	0.122	0.004	0.112	0.114	**0.00034**	0.00017

Sensitivity Analysis

c_d ~ Spinning apparatus

Plots below illustrate variation in PGLS model estimates due to phylogenetic uncertainty (across 100 trees) for c_d against spinning apparatus (see Tab. S6.1 for details). Histograms show the distribution of estimates (left) and P values (right), the red vertical line indicates average values across models. These results demonstrate that cribellar species have a significant lower c_d in comparison with ecribellar species across all PGLS models. Therefore, results are highly robust to phylogenetic uncertainty.

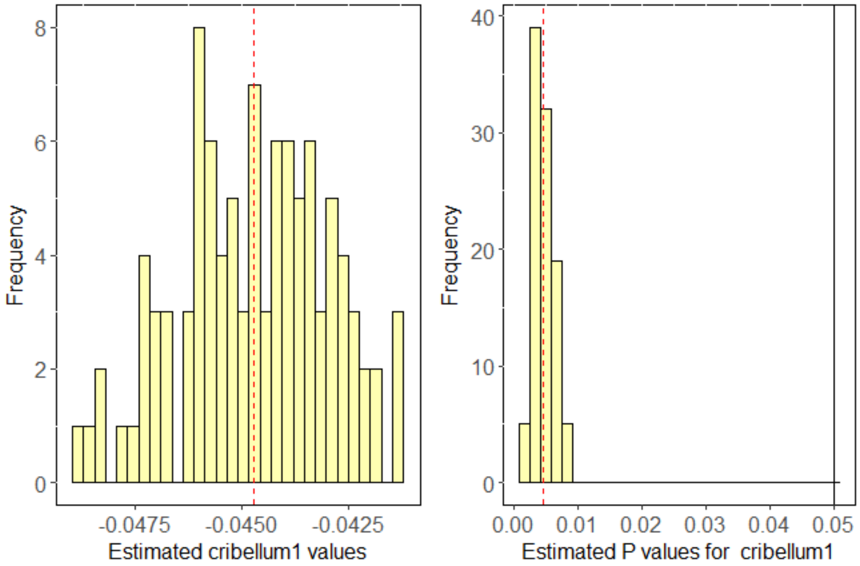

h_r ~ Spinning apparatus

Plots below illustrate variation in PGLS model estimates due to phylogenetic uncertainty (across 100 trees) for h_r against spinning apparatus (see Tab. S6.1 for details). Histograms show the distribution of estimates (left) and P values (right), the red vertical line indicates average values across models. These results demonstrate that cribellar species have a significant lower h_r in comparison with ecribellar species across all PGLS models. Therefore, results are highly robust to phylogenetic uncertainty.

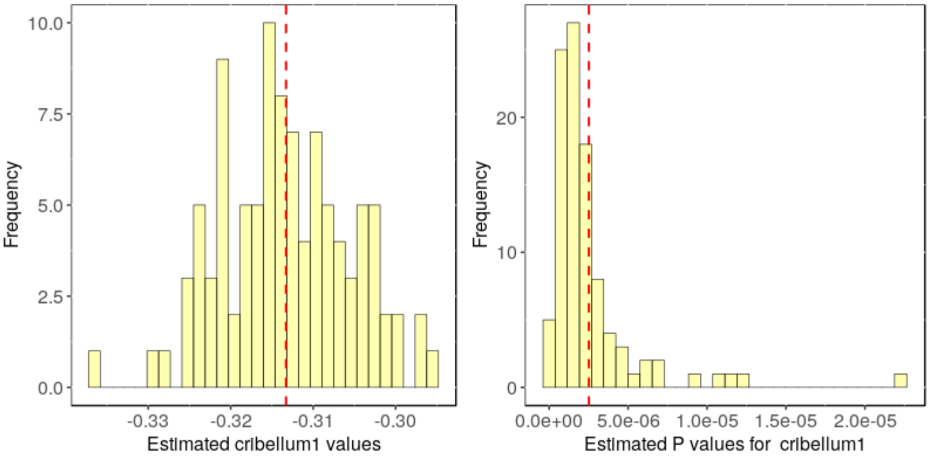

c_d ~ Web Type

Plots below illustrate variation in PGLS model estimates due to phylogenetic uncertainty (across 100 trees) for c_d against *Web Type* (see Tab. S6.2 for details). Histograms show the distribution of estimates (left) and P values (right), the red vertical line indicates average values across models. Results below demonstrate that c_d of substrate builders is not different to the intercept (= web absent) ($P > 0.05$) across all PGLS models while c_d of aerial web builders (web_type_2) is significantly different to the intercept (= web absent) for nearly all PGLS models (across 100 trees). Therefore, results are robust to phylogenetic uncertainty, reinforcing that aerial webs show higher c_d.

Web_type_1 (substrate web)

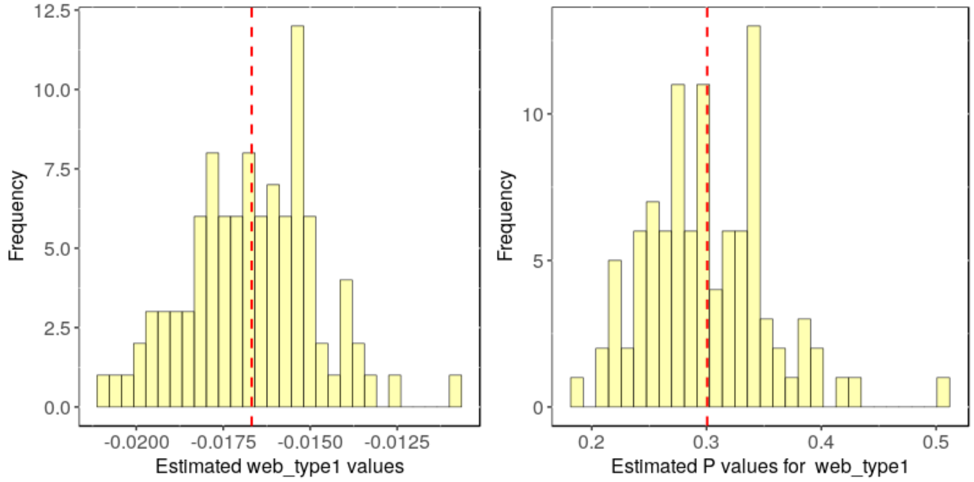

Web_type_2 (aerial web)

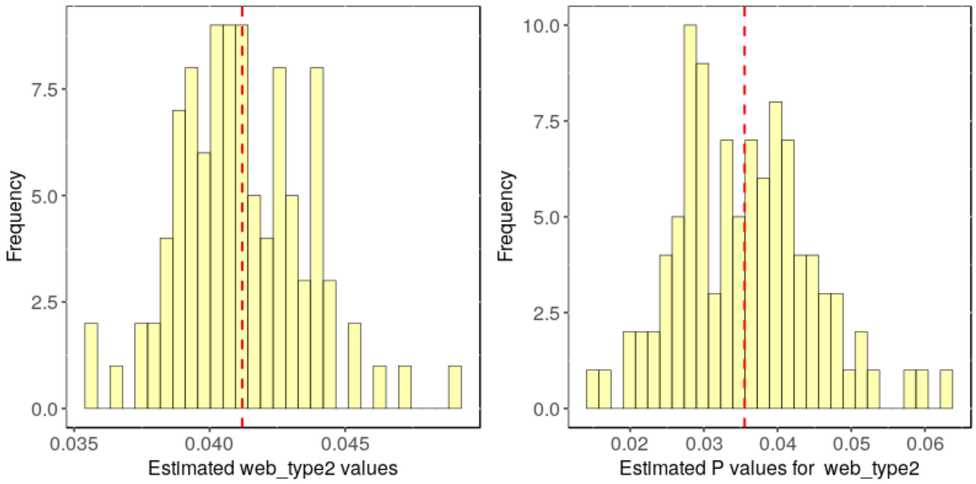

h_r ~ Web Type

Plots below illustrate variation in PGLS model estimates due to phylogenetic uncertainty (across 100 trees) for h_r against *Web Type* (see Tab. S6.2 for details). Histograms show the distribution of estimates (left) and P values (right), the red vertical line indicates average values across models. Results below demonstrate that h_r of substrate and aerial builders are not different to the intercept (= web absent) ($P > 0.05$) across all PGLS models. Therefore, results are robust to phylogenetic uncertainty, reinforcing that h_r did not correlate with web type.

Web_type_1 (substrate web)

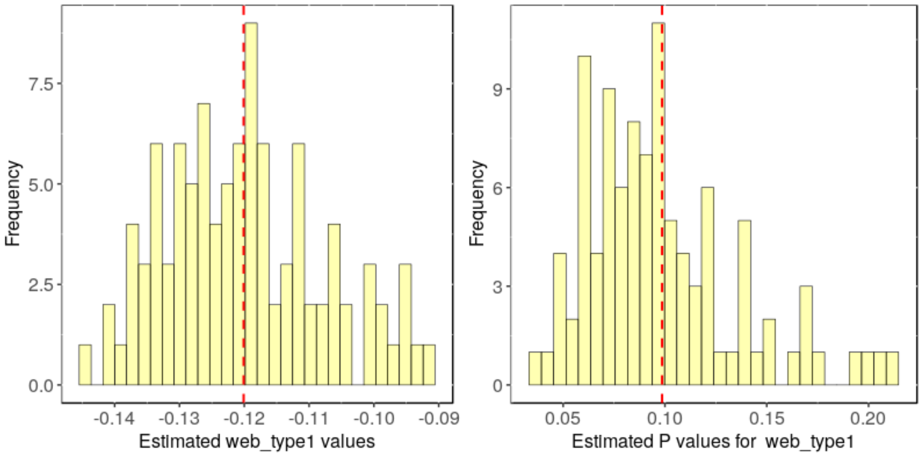

Web_type_2 (aerial web)

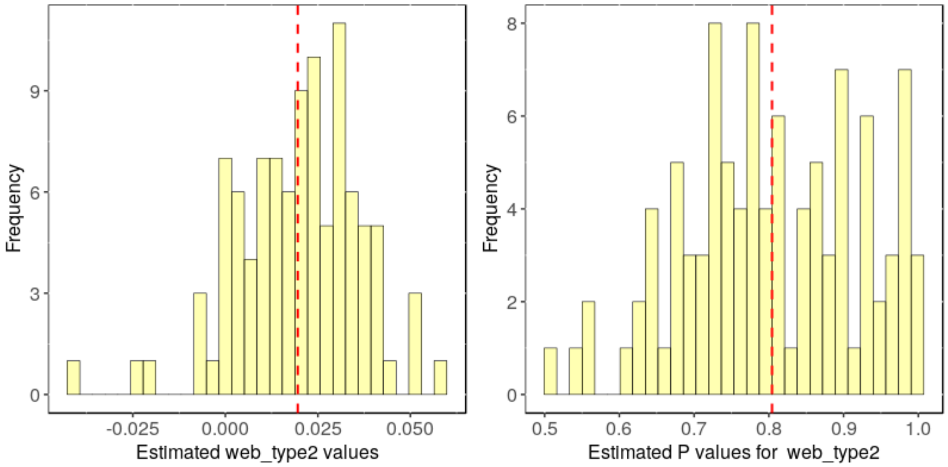

$c_d \sim h_r$

Plots below illustrate variation in PGLS model estimates due to phylogenetic uncertainty (across 100 trees) for c_d against h_r (see Tab. S6.3 for details). Histograms show the distribution of estimated slopes (left) and P values (right), the red vertical line indicates average across models. Results below demonstrate that the regression between c_d and h_r was significant ($P < 0.05$) for all PGLS models (across 100 trees). Therefore, results are robust to phylogenetic uncertainty, reinforcing that with c_d correlates with h_r .

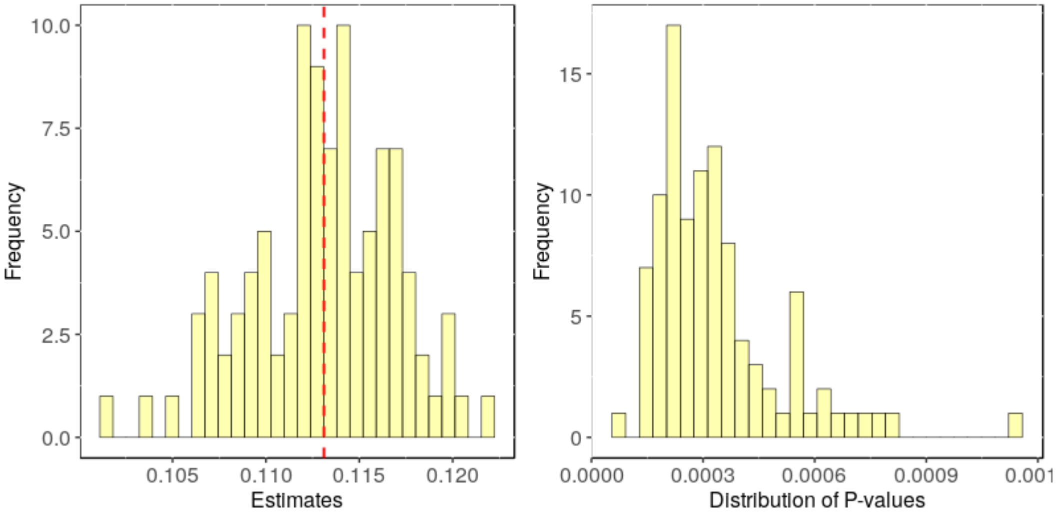

<u>ESM.8</u>. Geometric Morphometric PCMs on spinneret trajectory data with *geomorph*

GPA-Alignment

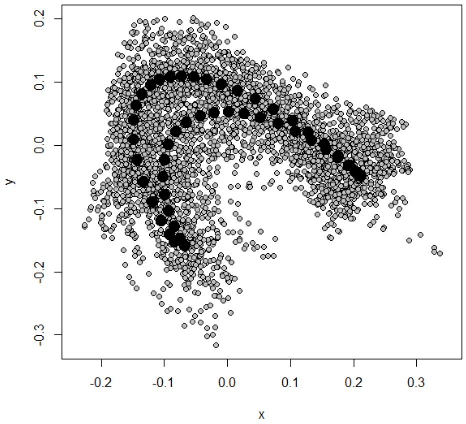

Phylogenetic signal

Spinneret-aligned:

```
Observed Phylogenetic Signal (K): 0.6847

P-value: 0.001

Based on 1000 random permutations
```

GPA-aligned:

```
Observed Phylogenetic Signal (K): 0.8007

P-value: 0.001

Based on 1000 random permutations
```

Phylo-Morphospace

Spinneret-aligned:

GPA-aligned:

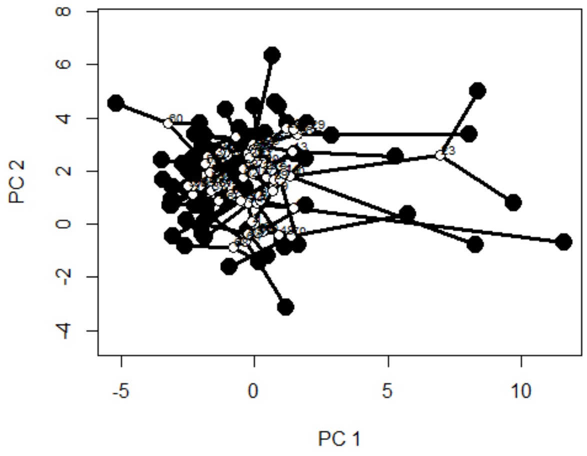

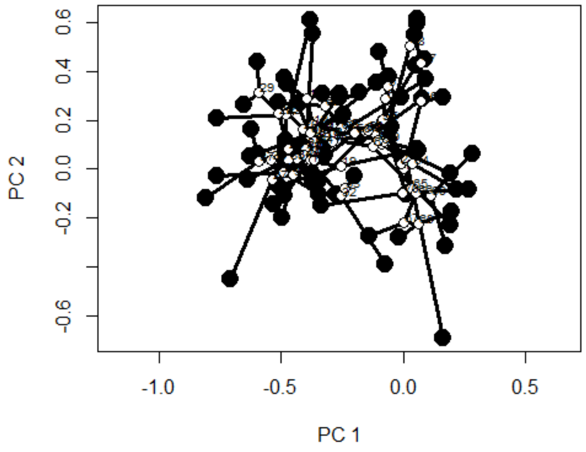

Comparing track shapes between groups

Cribellar vs. ecribellar

Spinneret-aligned:

```
procD.pgls(f1 = A ~ cribx, phy = treex, iter = 999)

Type I (Sequential) Sums of Squares and Cross-products
Randomized Residual Permutation Procedure Used
1000 Permutations
ANOVA effect sizes and P-values based on empirical F distributions


          Df     SS       MS     Rsq      F        Z Pr(>F)
cribx      1 0.0770 0.076955 0.00918 0.6394 -0.22243  0.585
Residuals 69 8.3049 0.120361 0.99082
Total     70 8.3819
```

GPA-aligned:

```
          Df       SS        MS     Rsq      F       Z Pr(>F)
cribx      1 0.001554 0.0015539 0.01643 1.1525 0.53222  0.316
Residuals 69 0.093034 0.0013483 0.98357
Total     70 0.094588
```

*Web types**

Spinneret-aligned(*):

```
procD.pgls(f1 = A ~ webx, phy = treex, iter = 999)

Type I (Sequential) Sums of Squares and Cross-products
Randomized Residual Permutation Procedure Used
1000 Permutations
ANOVA effect sizes and P-values based on empirical F distributions

          Df     SS      MS     Rsq     F      Z Pr(>F)
webx       2 0.5109 0.25546 0.06096 2.207 1.5808  0.059 .
Residuals 68 7.8710 0.11575 0.93904
Total     70 8.3819
```

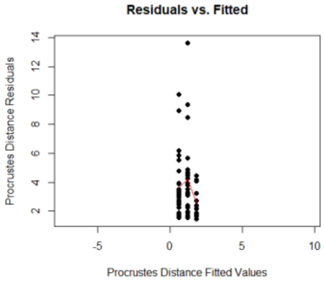

GPA-aligned**:

```
          Df       SS        MS    Rsq      F      Z Pr(>F)
webx       2 0.011057 0.0055287 0.1169 4.5008 3.2716  0.002 **
Residuals 68 0.083530 0.0012284 0.8831
Total     70 0.094588
```

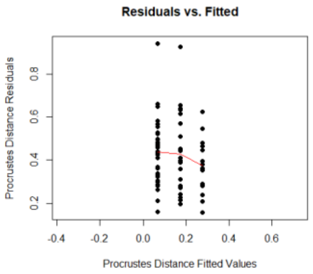

Centrality(*)

Spinneret-aligned*:

```
procD.pgls(f1 = A ~ centrx, phy = treex, iter = 999)

Type I (Sequential) Sums of Squares and Cross-products
Randomized Residual Permutation Procedure Used
1000 Permutations
ANOVA effect sizes and P-values based on empirical F distributions

          Df     SS      MS     Rsq      F      Z Pr(>F)
centrx     1 0.9031 0.90308 0.10774 8.3319 3.2017  0.001 **
Residuals 69 7.4788 0.10839 0.89226
Total     70 8.3819
---
Signif. codes:  0 ‘***’ 0.001 ‘**’ 0.01 ‘*’ 0.05 ‘.’ 0.1 ‘ ’ 1
```

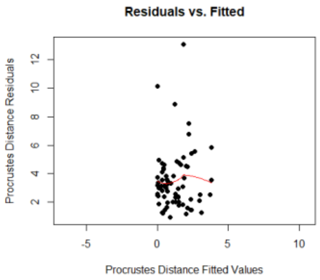

GPA-aligned:

```
          Df       SS        MS     Rsq      F       Z Pr(>F)
centrx     1 0.001512 0.0015122 0.01599 1.1211 0.51745  0.301
Residuals 69 0.093075 0.0013489 0.98401
Total     70 0.094588                                     ---
Signif. codes:  0 ‘***’ 0.001 ‘**’ 0.01 ‘*’ 0.05 ‘.’ 0.1 ‘ ’ 1
```

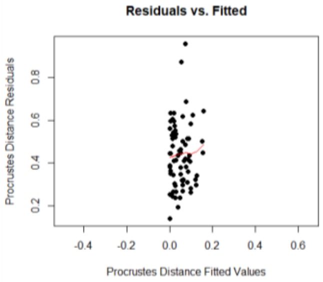

Comparing evolutionary rates

Cribellar vs. ecribellar*

Spinneret-aligned*:

```
Observed Rate Ratio: 1.9277
P-value: 0.014
Based on 1000 random permutations
The rate for group no is 0.000945749418143697
The rate for group yes is 0.00182315706480094
```

GPA-aligned*:

```
Observed Rate Ratio: 1.5286
P-value: 0.135
Based on 1000 random permutations
The rate for group no is 1.1671141266508e-05
The rate for group yes is 1.78408875444222e-05
```

Web types(*)

Spinneret-aligned*:

```
Observed Rate Ratio: 3.0715
P-value: 0.001
Based on 1000 random permutations
The rate for group aerial is 0.000497090342255345
The rate for group basic is 0.00152680602048892
The rate for group none is 0.00121867711186004
```

GPA-aligned:

```
Observed Rate Ratio: 1.1937
P-value: 0.521
Based on 1000 random permutations
The rate for group aerial is 1.16577994359458e-05
The rate for group basic is 1.34765955897021e-05
The rate for group none is 1.3916021907465e-05
```